Spring 1991

Analytical Modeling and Simulation for Investigation of a Digital Gas Filter Correlation Radiometer

Catherine P. McGowan
Old Dominion University

Recommended Citation

McGowan, Catherine P.. "Analytical Modeling and Simulation for Investigation of a Digital Gas Filter Correlation Radiometer" (1991). Master of Science (MS), Thesis, Electrical & Computer Engineering, Old Dominion University, DOI: 10.25777/z2cn-c707
https://digitalcommons.odu.edu/ece_etds/432

ANALYTICAL MODELING AND SIMULATION FOR INVESTIGATION OF A DIGITAL GAS FILTER CORRELATION RADIOMETER

by

Catherine P. McGowan
B.S. May 1987, Old Dominion University

A Thesis Submitted to the Faculty of
Old Dominion University in Partial Fulfillment
of the Requirements for the Degree

MASTER OF SCIENCE

OLD DOMINION UNIVERSITY
May, 1991

Approved By:

John W. Stoughton

Seong Ho Park

Linda L. Vahala

ABSTRACT

ANALYTICAL MODELING AND SIMULATION FOR INVESTIGATION OF A DIGITAL GAS FILTER CORRELATION RADIOMETER

Catherine P. McGowan
Old Dominion University
Director: John W. Stoughton

This thesis investigates a digital gas filter correlation radiometer called the Tropospheric Radiometer for Atmospheric Chemistry and Environmental Research (TRACER), which will be used to remotely measure carbon monoxide at three levels in the troposphere. The nadir-viewing radiometer measures the differential absorption of radiation through the atmosphere at 4.67μm and 2.33μm wavelengths. This thesis develops an analytical model of the TRACER measurement process to evaluate the effect of varying certain system parameters on the measurement. The independent sampling criterion and the response of linear systems to random signals are explained. A parametric simulation model is also developed to evaluate the analytical model.

The inputs to the model are the expected radiation onto the detectors at 4.67μm and 2.33μm calculated from previous atmospheric studies. The detector, preamplifier, analog-to-digital converter, and pulse averaging strategy are described in detail. The varied parameters are preamplifier cutoff frequency, quantization length, and sampling frequency.

TABLE OF CONTENTS

LIST OF TABLES

Page

LIST OF FIGURES

Figure Page

SYMBOL DEFINITIONS

λ	spectral wavelength
F_b	simulation base frequency
F_c	filter cutoff frequency
F_s	sampling frequency
Δ	differential signal, vacuum - gas
E_e	incident energy on the detectors
I_p	photocurrent
q	electronic charge
V	bias voltage
T	absolute temperature of the detector
η	quantum efficiency of the detector
k	Boltzmann's constant or gain
h	Planck's constant
c	speed of light
R_D	detector dynamic resistance
C_D	detector junction capacitance
Δf	noise bandwidth
R_F	feedback resistor
i_n	input current noise
e_n	input voltage noise

$H(s)$	transfer function
V_j	local average of vacuum cell
G_j	local average of gas cell
D_j	local differential average
$\mathbf{V}_k$	collective average of vacuum cell
$\mathbf{G}_k$	collective average of gas cell
$\mathbf{D}_k$	collective differential average
b	quantization length

CHAPTER ONE

INTRODUCTION

1.1 Background

Carbon Monoxide (CO) is a photochemically active gas which is distributed globally throughout the atmosphere and is a key component in the chemistry of the troposphere. The troposphere lies below the stratosphere and acts as a chemical cauldron, modifying surface emissions that can lead to pollution, greenhouse gasses, and compounds that are transported into the stratosphere and react there. Carbon monoxide is the second most abundant air pollutant found in the atmosphere, after carbon dioxide, and is principally man-made [1].

With increased industrialization and urbanization, the injection of man-made gaseous and particulate matter into the atmosphere has resulted in adverse effects on all aspects of human, animal, and plant life. Too little is known about the complex interaction of man-made and naturally produced air pollution with the atmosphere to evaluate the effects of pollution on a global scale. At the present time, several pollutants are believed to have an impact on the global radiation budget and thus on the global climate. These include increased concentrations of carbon dioxide, hydrocarbons, sulfur, nitrogen dioxide and carbon monoxide [1].

The study of CO distributions and chemical reactions in the troposphere is one important part of the whole effort to understand and minimize harmful effects of air pollutants.

It is anticipated that data of the multilevel global CO distribution will greatly enhance the knowledge of the various CO sources, better define global scale atmospheric circulation processes, and clarify the effects of these processes on tropospheric chemistry [2]. This in turn will increase our understanding of the Earth as an evolving system.

1.2 Need for Data About Carbon Monoxide

It is estimated that over half of the carbon monoxide in the atmosphere comes from human activities including motor traffic, other combustion of fossil fuels, and the burning of wood and rain forests [3]. Over the years these sources have increased gradually and have already caused the concentrations of CO to double since pre-industrial times. Prior to this, human activities did not significantly affect the global cycles of CO and other trace gasses. There is a positive correlation between increasing levels of CO and tropospheric ozone (O_3) and a build-up of many other trace gases in the atmosphere [1]. This may in turn cause widespread perturbations of tropospheric chemistry, global warming, and other climatic changes.

Because of the increased public concern about the deterioration of the ozone and the greenhouse effect, committees of the National Academy of

Sciences and the National Research Council have recommended the development of a chemical tracer model which combines chemistry and circulation models, as well as meteorological variables such as temperature, winds, etc., to better understand the photochemical and transport processes in the troposphere [1]. In the modeling of global tropospheric chemistry, emphasis has been placed on the problems of ozone (O_3), carbon dioxide (CO_2) and CO (the carbon cycle), the nitrogen cycle, and the sulfur cycle. CO is useful as a chemical tracer of atmospheric motions in four dimensions because it has a lifetime on the order of one to three months while longer lived gasses are more evenly distributed and thus do not reveal much about atmospheric mixing. Also, there is an active relationship between the long-term trend of CO and the changes in the concentrations of CO_2, methane (CH_4), hydroxyl (OH), and tropospheric O_3 [2]. The attainment of a data set on the global distribution and variability of CO is one important step if the validity of the chemical tracer model is to be properly determined.

The recent rates of increasing emissions in the globally averaged concentration of CO are between 0.8% and 1.4% per year and this increase exhibits an interhemispheric gradient of about a factor of three and concentrations are higher in the Northern Hemisphere (80-200ppbv) than in the Southern Hemisphere (30-60ppbv) [4]. It is estimated that over 200 million tons of carbon monoxide are emitted yearly by anthropogenic sources (85% of that from automobile exhaust) [3]. At the present rate of increase of global emission of CO from natural and combustion sources at the earth's surface, one would expect to see a gradual increase in atmospheric CO levels. However the observations available fail to indicate any such changes, indicating that the atmospheric concentration of CO may be in equilibrium. This implies that there must be major sinks for CO in the troposphere or at its boundaries.

Despite the numerous studies on the global budget and distribution of CO, there remains a great uncertainty in the magnitude of many of the sources and sinks of CO. The lack of data on the seasonally dependent sources and distribution of carbon monoxide is now and will continue to be a major obstacle to understanding tropospheric chemistry [1]. It has proven to be exceedingly difficult to obtain direct measurements of CO since theoretical models and numerical simulations such as the chemical tracer model must be used to define its global distribution. In particular, the development of realistic three dimensional combined chemistry and transport models are required if this understanding is to be achieved, and these models must describe the global CO distribution.

1.3 CO Measurement Technique

The technique of gas filter correlation radiometry (GFCR) is extensively used in atmospheric sensing experiments to measure trace gasses in the atmosphere. It exploits the principle of atomic absorption by gasses as its measurement mechanism. Although every experiment may implement this technique differently, the concept is the same.

In 1981 and 1984, a CO measuring experiment called Measurement of Air Pollution from Satellites (MAPS) was flown on the space shuttle which employed the GFCR technique [5]. MAPS provided nearly instantaneous global measurement of tropospheric CO concentrations in the middle troposphere and stratosphere. The measurements from the MAPS experiment indicate that there are significant longitudinal gradients in the distribution of CO, and that the spatial and temporal variability of CO is much more pronounced than was expected for a trace gas that has an atmospheric residence time of at least one month. MAPS showed the general features of its distribution yet there is great uncertainty as to how CO varies with latitude, altitude and season [5].

This thesis examines an experiment proposed at NASA Langley Research Center which will measure CO at two of its most prominent wavelengths. This experiment, called the Tropospheric Radiometer for Atmospheric Chemistry and Environmental Research experiment, TRACER, also uses the gas filter radiometric technique and is a continuation of the MAPS research. Measurements from TRACER will provide information on the presence of carbon monoxide at three or four levels in the atmosphere by measuring the strength of CO absorption lines at wavelengths of 4.67μm and 2.33μm while MAPS used only the 4.67μm wavelength.

To answer questions concerning the accumulation of air pollutants, the effects on the global heat balance and on global meteorology, the relationships between sources, routes, and reservoirs, and the role of air chemistry, measurements must be made over the entire surface of the earth. Satellites offer the opportunity to conduct global measurements, covering regions where it is impractical or insufficient to employ ground stations. Only satellite borne measurements systems are capable of achieving the fine temporal and spatial resolution required to define the distribution of this gas.

1.4 Overview of TRACER

TRACER is a passive remote sensor that measures molecular absorption of gasses between the earth and the sensor. For tropospheric measurements from space the downward-viewing (nadir) mode provides the widest vertical and horizontal coverage. These sources of radiation are relatively weak and require more sensitive detection instruments when compared to detection of direct solar radiation looking upward through the atmosphere, as in stratospheric solar occultation measurements.

To carry out the desired global scale studies of CO, it is estimated that a 5° latitude by 5° longitude (105km^2) Earth measurement scale will be sufficient. Two spectral channels are used to obtain the desired vertical resolution. The specified space platform on which TRACER will be flown has a 90 minute orbit at an altitude of 701km and a sixteen day repeat cycle. This provides sampling of each 5° by 5° grid square at least once every four days by the mid and upper troposphere channel ($\lambda = 4.6\mu\text{m}$) and once every twelve days in the mixing layer channel ($\lambda = 2.3\mu\text{m}$). It is expected that the instrument will be capable of measuring an absolute radiance accuracy of ±3% in the 4.6μm spectral channel and ±10% in the 2.3μm spectral channel.

Figure 1.1 shows a block diagram of the TRACER gas correlation radiometer. As radiation passes through the atmosphere, it undergoes selective absorption and emission that varies depending on the composition, temperature, and pressure of the atmosphere. A sample of this upwelling radiation, measuring an earth footprint of 15km diameter (176km^2), is collected by the instrument telescope and is optically directed to a system of gas filled cells. These gas cells are mounted on a rotating chopper wheel which acts as a mechanical modulator. The detectors receive the modulated energy and produce a current proportional to the input energy.

Because the gas in the cells acts as a highly selective spectral filter, there is a difference in the energy transmitted to the detection system between the gas and evacuated cells. When the target gas is present in the atmosphere, a spectral component of the incoming solar energy correlates with the absorption line spectrum of the identical gas in the cell and that spectral component is attenuated, ie. it is absorbed out. Energy passing through an evacuated cell provides a measure of scene brightness. The difference between the signals through a gas filled cell and a vacuum cell relates to the amount of gas in the atmosphere with absorption features that correlate with those of the gas in the cell. Also, the altitude of the gas in the atmosphere is related to the pressure of gas in the cell. Combining the scene brightness measurement, the difference signal, and

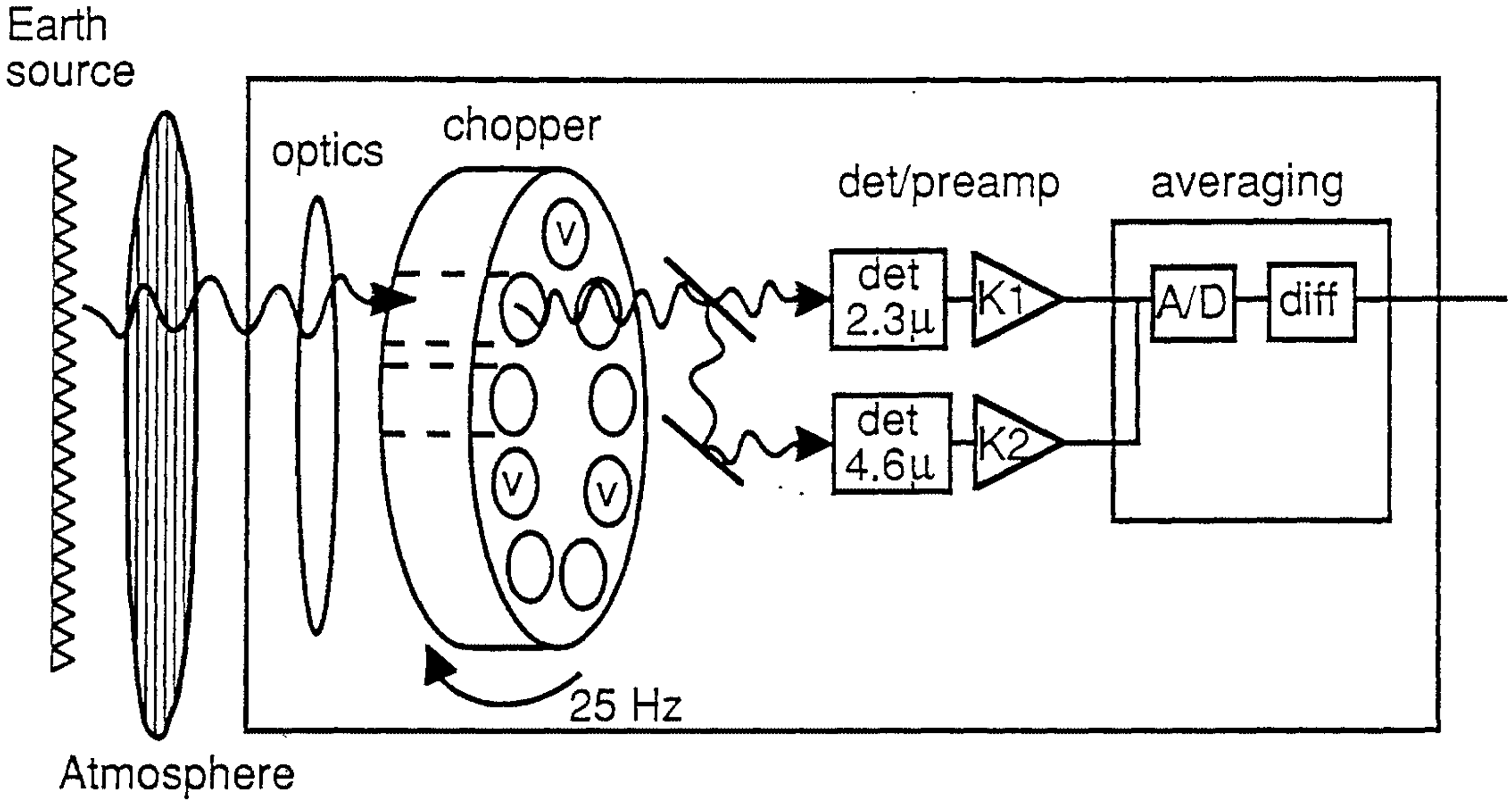

cells: CO, CO, vac, CO, calib, vac, N_2O, CH_4, vac

Figure 1.1. Block Diagram of TRACER Instrument.

knowledge of certain atmospheric parameters such as temperature profile and barometric measurements, the atmospheric mixing ratio of CO can be inferred.

The values recorded by TRACER for both channels include the measured average of each vacuum and gas cell signal and the differential between pairs of vacuum and gas cells, the average of 64 vacuum cells and gas cells (64 chopper revolutions), and the average over 64 of the signal differentials. The averages over 64 chopper revolutions are telemetered directly to earth for instrument monitoring and control. All of the sampled values are stored in the flight computer for transmission to earth at a later time for more detailed evaluation. The averages over 64, a duration of approximately 2.56 seconds, provide a completely new Earth footprint.

1.5 Thesis Research Objective

In the past, the GFCR technique for measuring trace gasses has been realized entirely with analog circuitry. Although these systems perform well, they exhibit measurement errors due to low frequency noise from temperature sensitive drift and electronic crosstalk. Electronic crosstalk due to non-ideal, higher harmonics of demodulation waveforms has been observed in similar experiments and is difficult to eliminate. Digital processing allows many analog functions to be done easily and with greater flexibility.

The purpose of this thesis to develop both an analytical model and a simulation model to investigate a digital processing approach for measuring trace gasses in which samples from the amplifier output are quantized and averaged to obtain an estimate of the measurement. TRACER is one of the first GFCR projects proposed at LaRC to use the sample and average averaging method as part of the original design. It is desired to determine a tolerance limit for the measurement error. The effect of changing various parameters such as sampling frequency and quantization length will be investigated by analysis and simulation. The simulation results will be compared to the analytical results.

The first step in developing the simulation model is to provide an accurate parametric representation of the measurement process. This model is implemented using custom software or other CAED packages. Through simulation, performance aspects and engineering trade-offs of the digital processing method can be evaluated based on parameter variation. The parameters of interest in this investigation are the preamplifier cutoff frequency, the sampling frequency, and the quantization length.

A detailed description of the measurement technique of GFCR as employed by TRACER is discussed in Chapter Two. Assumptions made for the models are also given. The analytical model is described in Chapter Three and includes development of the simulation model. The simulation plan is presented in Chapter Four along with results of the simulation tests and related design issues. Conclusions and plans for future research are given in Chapter Five.

CHAPTER TWO

RADIOMETER MODEL

2.1 Introduction

The National Aeronautics and Space Administration is conducting a number of experiments to measure various atmospheric constituents and global tropospheric chemistry. These experiments are in response to the need for atmospheric research as discussed in Chapter One. This thesis examines one experiment, Tropospheric Radiometer for Atmospheric Chemistry and Environmental Research experiment (TRACER) through analytical modeling and simulation. TRACER is designed to measure the global distribution of carbon monoxide concentrations at three or four levels vertically through the troposphere. This experiment uses the technique of gas filter correlation radiometry (GFCR) which is widely used to determine the presence of trace gasses in the atmosphere.

This chapter will address the TRACER model with emphasis on components which are of interest to our investigation; namely, the optics and mechanical chopper, the detector and preamplifier, and the signal processing method. Pertinent parameters of each subsystem are incorporated into component models to evaluate the experiment through simulation. The objective is to determine tolerance limits for the measurement error and to compare the estimates of several sets of parameters to optimize radiance measurements with respect to the selected parameters.

2.2 Simulation Model

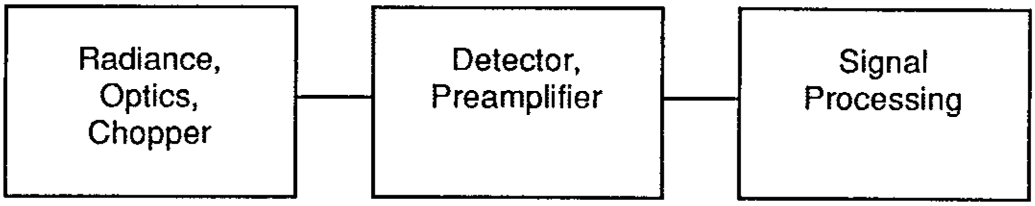

The model is broken into three modules for analysis and simulation as shown above. These are the input radiance, optics and chopper, the detector and preamplifier, and the signal processing.

2.2.1 Input Radiance

Radiation at the entrance pupil of the sensor is composed of thermal and solar radiation transmitted through the atmosphere. Since the instrument must "look" through 13 layers of atmosphere, the amount of energy collected by the instrument will be very small. At the 4.67μm wavelength, the energy is mostly thermal energy and depends primarily on the temperature of the portion of Earth in view. The thermal infrared radiation detected within the 4.67μm fundamental spectral absorption band of CO limits measurements to the middle and upper troposphere. To obtain data in the mixing region, TRACER will also use the 2.33μm CO absorption band. At 2.33μm, the solar terms are about 5 orders of magnitude greater than the thermal terms and depend on the reflectivity of the portion of Earth in view and the angle of the Sun. The energy collected at the 2.33μm wavelength will be much less than the energy collected at the 4.67μm wavelength.

2.2.2 Optics and Chopper

The optical focusing is fairly simple comprised primarily of mirrors with highly reflective surfaces. Figure 2.1 shows the TRACER optical schematic. The In-Flight-Calibration blackbodies, the calibration gas cells and the chopper gas cells are inserted into the optical focal path at the focal point.

Following the chopper, a dichroic beamsplitter divides the 2.33μm and 4.67μm spectral energy and directs it through separate bandlimiting spectral filters and relay lenses which focus the energy onto the detectors. The interference filters spectrally filter the radiant energy between λ_{min} and λ_{max}. The 2.33μm channel spectral bandpass region is 2.33μm ±4% and the 4.67μm spectral bandpass is 4.67μm ±3%. The optical components are assumed to be stationary with no imperfections.

As shown in Figure 2.2, the chopper is divided into nine segments, providing for three vacuum cells, five gas cells and a thermally controlled high emissivity calibration patch. A vacuum cell is located next to every gas cell so that the reference measurement is as close as possible, spatially, to the gas cell from which it is differenced. Thus, minimal radiant error is introduced into the difference signal. The calibration patch is thermally controlled and provides a radiant

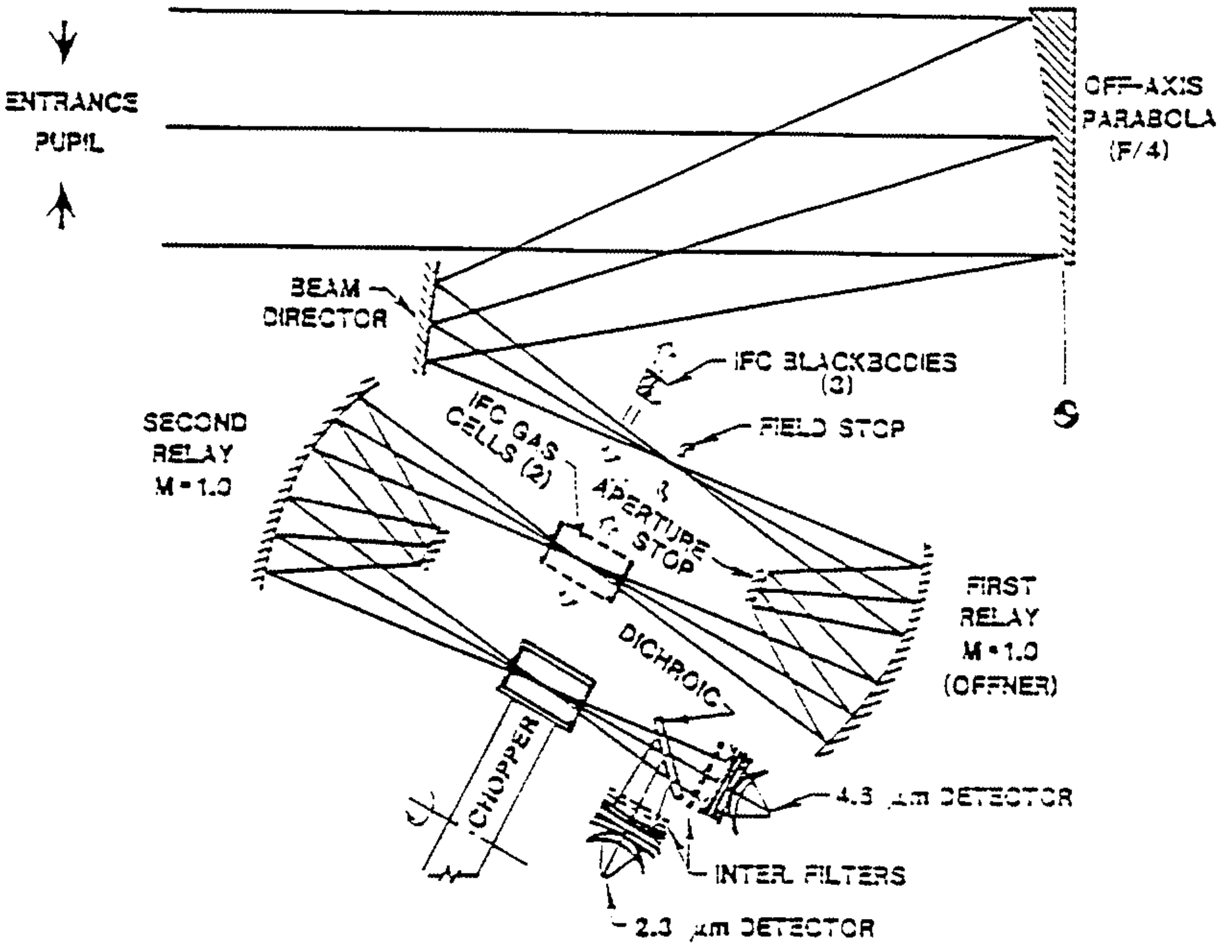

Figure 2.1. TRACER Optical Schematic.

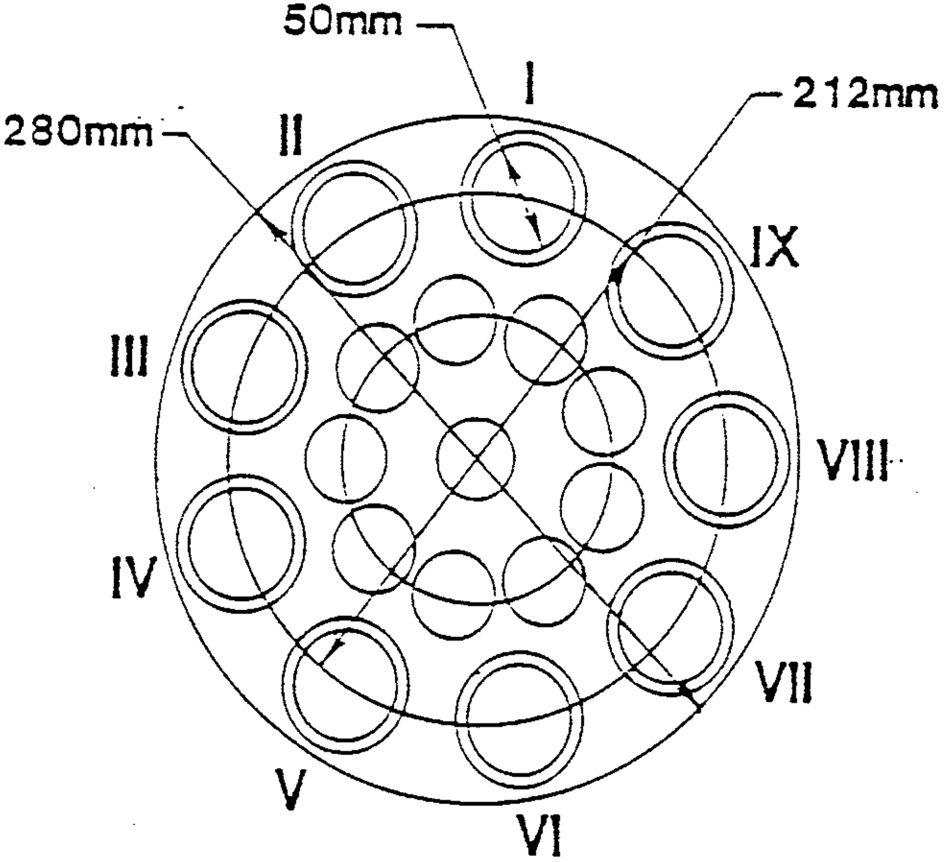

WHEEL POSITION	GAS CELL/PATCH		
	GAS	PRESSURE (hPa)	LENGTH (mm)
I	CO	350	50
II	CO	100	50
III	VAC	0	10
IV	CO	100	10
V	WHEEL CALIBRATION PATCH		
VI	VAC	0	10
VII	N_2O	350	50
VIII	CH_4	350	10
IX	VAC	0	10

Figure 2.2. TRACER Gas Cell Chopper Wheel Layout.

reference for the data. In order to correct for systematic and some random errors in the measurement, nitrous oxide (N_2O) in the 4.67μm region and methane (CH_4) in the 2.33μm region are also measured. Among other things, these channels facilitate the removal or correction of cloud contaminated data.

Each cell has a diameter of 50mm with its center located on a circle of 106mm radius. To obtain the desired resolution, the sequential vacuum cell and gas cell views must occur within approximately 5ms. A chopper wheel rotational speed of 25rps as proposed in the baseline design allows the background scene stability criteria between vacuum cell and gas cell views to be met for most Earth terrain variations. This provides a measurement every 4.4ms.

The size and shape of the radiation focused onto the chopper wheel affects the shape of the modulation waveform. The radiation geometry is assumed to be a circular spot on the chopper wheel which remains constant in size and shape based on the assumption that the optics are stationary. The chopper waveform is modeled by computing the area between two circles, one representing the energy spot with diameter 21mm and the other representing a cell with a 50mm diameter, as one "slides past" the other. The shape of the modulating chopper waveform was calculated with the MathCAD software package. The chopper waveform is shown in Figure 2.3 and was generated at 1333 points per pulse or a frequency of 299.925kHz. This frequency is referred to as the simulation base frequency, F_b.

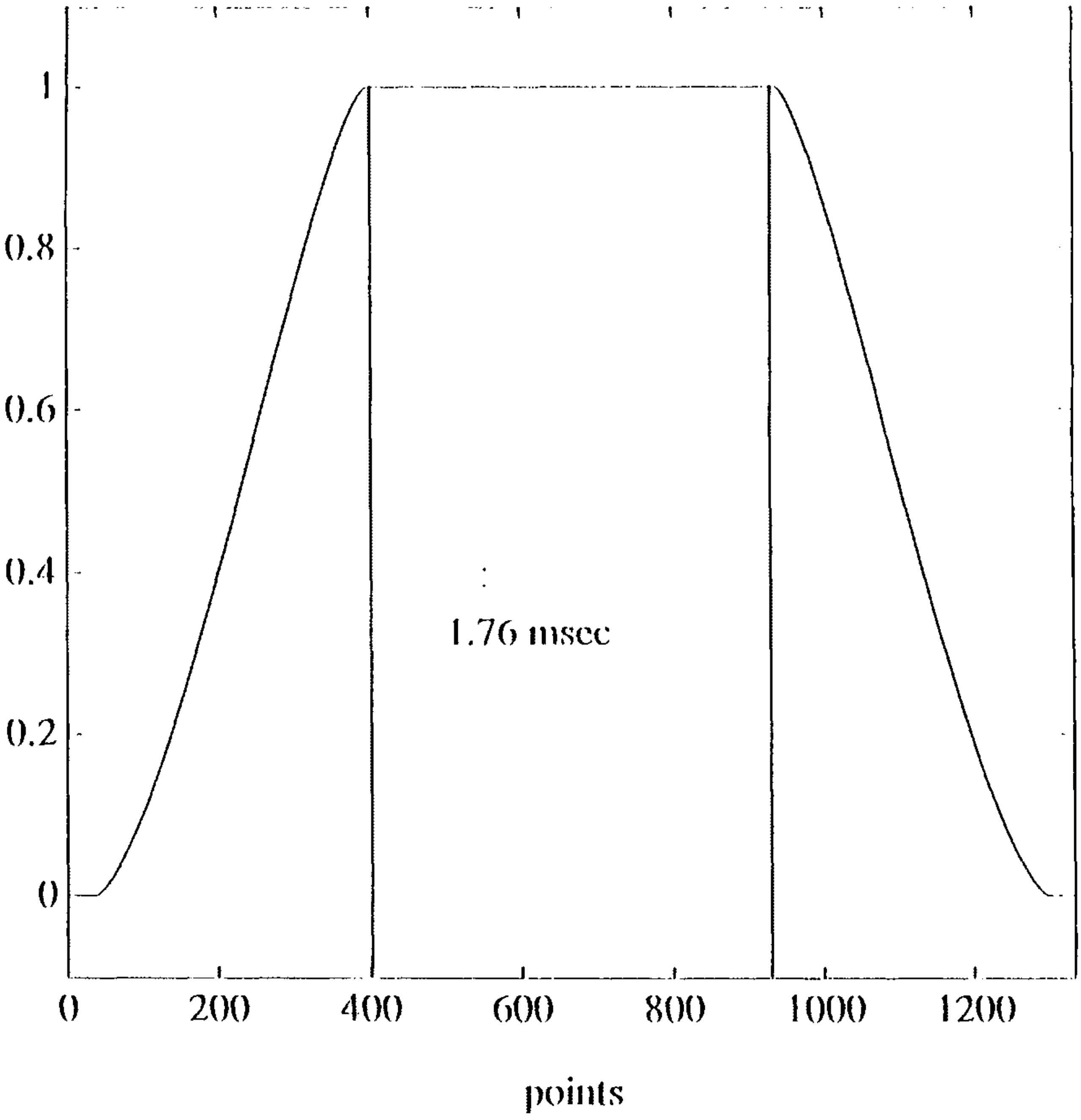

Figure 2.3. Normalized Chopper Waveform.

The chopper wheel is enclosed in a temperature controlled shroud which thermally stabilizes the chopper wheel and cells. The chopper's speed and position will be monitored in order to provide both motor speed control and position pickoffs to key the digital sampling of the detector as each cell passes through the optical beam. The chopper temperature and speed are assumed to remain constant.

The power incident on the detectors for both channels were determined by the TRACER staff. Since signal values vary greatly between channels, extreme cases are used in the simulation. These extreme cases consist of the maximum signal and maximum differential value on the 4.67μm channel since it has the larger expected signal value, and the minimum signal and minimum differential value on the 2.33μm channel. These radiant powers, tabulated in Table 2.1, include the effects of the optical components. The differential value is the power transmitted through the vacuum cell minus the power transmitted through the gas filled cell. This 'true' radiant differential, with units of watts, will be referred to by Δ_W. It is assumed that the energy collected for each channel during 64 chopper revolutions is constant.

Table 2.1 Radiance Values onto the Detectors.

	4.67μm (W)	2.33μm (W)
vacuum cell	$1.433 \cdot 10^{-6}$	$3.698 \cdot 10^{-8}$
gas cell	$1.698 \cdot 10^{-6}$	$3.688 \cdot 10^{-8}$
spoke	$2.024 \cdot 10^{-6}$	$6.552 \cdot 10^{-9}$
difference, Δ_W	$-2.643 \cdot 10^{-7}$	$1.020 \cdot 10^{-10}$

2.2.3 Detector and Preamplifier

The detectors needed for this experiment must be able to detect very small signals, on the order of 10^{-6} to 10^{-8} watts. Indium Antimonide (InSb) is an intrinsic photovoltaic (PV) detector which is sensitive to wavelengths from 1μm to 5.5μm. It produces a current proportional to the incident energy integrated over a spectral bandwidth. The detector is made of adjacent zones of p and n doped material to form a diode. At 77K, the bandgap of InSb is .22eV. Cooling the detector minimizes thermal noise and improves the detectivity of the detectors. Photons of energy > .22eV ($\lambda < 5.5\mu$m) are absorbed at the junction to create an electron-hole pair. These are separated by the junction field and appear as charge at the electrodes.

Photovoltaic devices are commonly operated as current generators. For an incident energy, E_e (W), the total photocurrent, I_p (A), is given by the equation below [6]:

$$I_p = I_0[e^{qV/kT} - 1] - q\eta E_e\lambda/hc \qquad \text{(A)}$$

where q is the electronic charge, k is Boltzmann's constant, h is Planck's constant, c is the speed of light, λ is wavelength, V is the bias voltage, T is the absolute temperature, and η is the quantum efficiency. The quantum efficiency is the number of electrons generated per incident photon and is essentially independent of wavelength for each channel. The photovoltaic detectors are operated into a virtual short circuit (bias voltage = 0V) so that the photocurrent becomes a linear function of the magnitude of the irradiance. The photocurrent equation then becomes

$$I_p = -\,q\eta E_e\lambda/hc \qquad \text{(A).}$$

With λ in μm, the equation for the photocurrent is

$$I_p = -\,.804\cdot E_e\eta\lambda \qquad \text{(A).}$$

The term $.804\cdot\eta\lambda$ is commonly referred to as the current responsivity. Although the current responsivity increases with wavelength until the maximum wavelength is reached, the photon responsivity is constant over this range. Thus, as desired, the incident radiation generates a current proportional to the number of detected photons.

Photon noise associated with background radiation is often the dominant source of noise. Since the measurement is the mean radiation incident upon the detector zero background noise is assumed and the detector produces only Johnson noise. Radiation contributes photon shot noise if the preamplifier keeps the diode bias zero. The equivalent circuit for the detector is shown in Figure 2.4. R_D is the junction resistance also called the dynamic impedance and C_D is the junction capacitance.

Associated with the photocurrent is a shot noise given by

$$i_{shot} = (2qI_p\Delta f)^{1/2} \qquad \text{(A)}$$

where Δf is the noise bandwidth. The equivalent current generator for the detector Johnson noise is

$$i_{det,J} = (4kT\Delta f/R_D)^{1/2} \qquad \text{(A).}$$

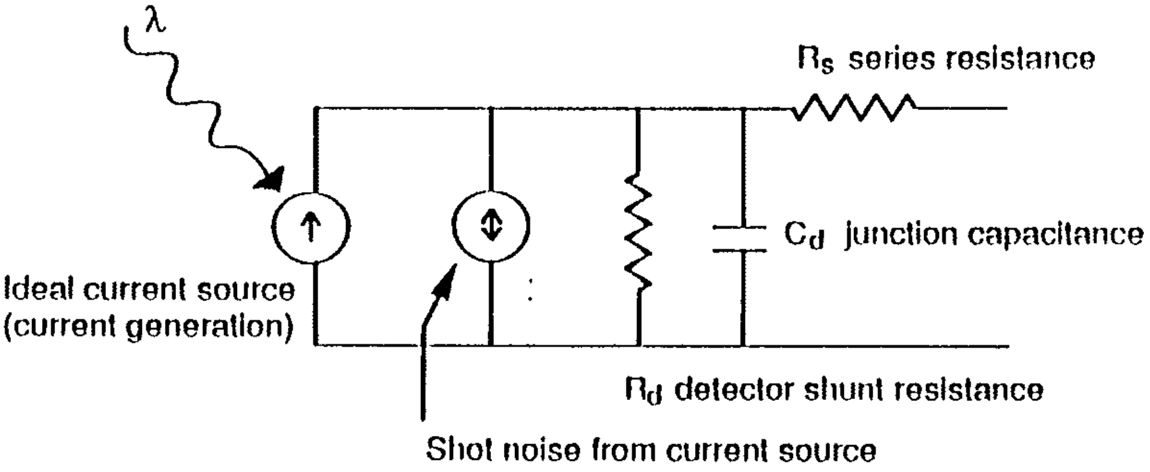

Figure 2.4. Detector Equivalent Circuit.

Amplification of the short-circuit current is commonly performed using a transimpedance amplifier. The output of the transimpedance amplifier is a voltage signal. The preamplifier electronics are located within the optics unit close to the detectors to minimize stray capacitance and line noise on the low output signal from the detectors and are cooled to the same temperature as the detectors. They must be designed to achieve Johnson noise limited operation. The transimpedance amplifier circuit shown in Figure 2.5 holds the voltage across the detector near zero where it has its maximum detectivity.

Noise sources associated with the preamplifier are Johnson noise due to the feedback resistor, R_F, input current noise, i_n, and input voltage noise, e_n. Input voltage noise is dominant at high frequencies (> 20kHz) and is considered negligible for this application. The input current noise is dominant at lower frequencies and is typically $< 5 \cdot 10^{-15} \mathrm{A}/\sqrt{\mathrm{Hz}}$ at frequencies less than 10kHz. The Johnson noise associated with R_F is

$$i_{pre,J} = (4kT\Delta f/R_F)^{1/2} \qquad (A).$$

The rms noise level is defined to be the square root of the noises added in quadrature.

$$i_{rms,total} = (i^2_{shot} + i^2_{det,J} + i^2_n + i^2_{pre,J})^{1/2} \qquad (A).$$

The noise varies linearly with the square root of the noise bandwidth as is evident from the noise equations. The Johnson noise terms contribute more than 99% of the total noise and varies inversely to resistance and directly to temperature.

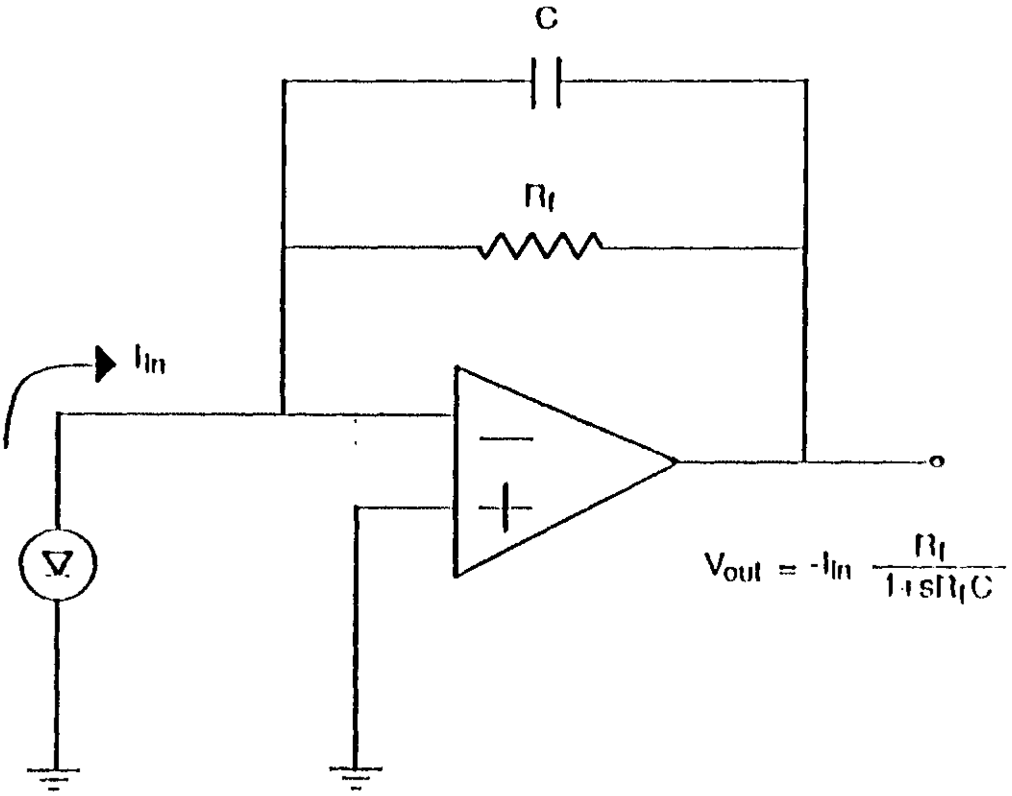

Figure 2.5. Transimpedance Amplifier Circuit.

Additional types of noise such as temperature noise and low frequency $1/f$ noise are not included. The $1/f$ noise is the least understood noise source. Several theories of its origin include the effect of the velocity of electrons through the lattice structure, electronic transitions involving surface states, and the electrical contacts to the detector [6]. It can usually be eliminated by specialized surface treatments. It is assumed that low frequency noise can be sufficiently eliminated with a highpass filter located between the two stages of the preamplifier. This effect is not modeled in this study.

A P-N junction photovoltaic device has a frequency response determined by the characteristics of the device itself and by the circuit in which it is operated. As seen from the equations, the dominant noise sources are dependent upon noise bandwidth. The noise bandwidth was determined empirically by the TRACER staff to be 13.5kHz for filter cutoffs up to 20kHz using an equivalent resistance and capacitance to model the detector. The noise bandwidth is assumed constant to over the passband frequencies. To obtain the noise power, the noise power spectrum is integrated over the noise bandwidth.

A two pole Butterworth Impulse Invariant design is used to obtain the filter coefficients for the amplifier stage. This design method was chosen since the output of an invariant impulse digital filter is the same as samples of an analog filter with the same transfer function. If the analog filter is bandlimited, lowpass, and the cutoff frequency is sufficiently low, then the digital filter frequency response will closely approximate the analog frequency response and aliasing effects are not significant [7]. The two pole normalized Butterworth transfer function is:

$$H(s)=\frac{1}{s^2+\sqrt{2}s+1}$$

The digital transfer function is found by using the Laplace transform to get to the time domain and then using the z transform to get the desired transfer function:

$$H(z)=\frac{z^{-1}\sqrt{2}T\exp(-\frac{T}{\sqrt{2}})\sin(\frac{T}{\sqrt{2}})}{1-z^{-1}2\exp(-\frac{T}{\sqrt{2}})\cos(\frac{T}{\sqrt{2}})+z^{-2}\exp(-\sqrt{2}T)}$$

This is the normalized equation and T is found from relationship:

$$T = 2\pi \cdot F_c/F_b$$

where F_b is the base sampling frequency and F_c is the desired filter cutoff frequency.

The main amplification stage consists of a two stage amplifier with a highpass RC filter between the stages to eliminate dc bias and $1/f$ noise. It is assumed that no additional noise is added here. This stage is used as an adjustable gain to raise the output signal to a level suitable for sampling. The gain is selected for each channel such that the largest signal at the A/D input is seven volts. Parameters for the InSb PV detector and preamplifier obtained from Cincinnati Electronics and EG&G Judson through both private conversation and data sheets, and as designated in the TRACER instrument announcement are given in Table 2.2.

Table 2.2 TRACER Parameter Values.

$\eta = .6 - .8$
$T_D = 100 - 120$ K
$R_D = 8 - 10$ kΩ
$C_D = 6$ nF
$i_n = 5 \cdot 10^{-15}$ A
$R_F = 3.2$ kΩ

2.2.4 Signal Processing

After passing through the amplifier, the signal looks like a series of pulses. It is the pulse peaks which contain the radiance information. The measurements of interest are the average value of each gas and vacuum pulse height, the difference between vacuum and gas cell average values, and the average of 64 chopper cycle difference values. The mean differential detector output represents the radiation power in the wavelength band.

Below are defined the various averages used in the subsequent analysis. The local averages are sample averages over one pulse, either a vacuum or a gas pulse. The collective average is the average of 64 local averages. Here, i is the index for either a gas or vacuum cell pulse and j indexes the pulse pairs. For a vacuum cell view, the local average is

$$V_j = 1/m \cdot \sum v_i \qquad = 1 \text{ to } m$$

where v_i represents a sample from a vacuum cell view and m is the number of samples. Similarly, the local average for a gas cell is

$$G_j = 1/m \cdot \Sigma g_i \qquad = 1 \text{ to } m$$

where g_i represents a sample from a gas cell view. For one pulse pair, the local differential average between a vacuum cell view and a gas cell view is

$$D_j = V_j - G_j.$$

The collective average over 64 pulse pairs for the vacuum and gas cells are designated $\mathbf{V_k}$ and $\mathbf{G_k}$ respectively where

$$\mathbf{V_k} = 1/64 \cdot \Sigma V_j \qquad j = 1 \text{ to } 64$$

and

$$\mathbf{G_k} = 1/64 \cdot \Sigma G_j \qquad j = 1 \text{ to } 64.$$

The collective differential over 64 pulse pairs is

$$\mathbf{D_k} = \mathbf{V_k} - \mathbf{G_k}.$$

A fixed integration time is predetermined by the chopper waveform and preamplifier cutoff. The integration time is established when all instrument transient responses have settled out so that a true radiant measurement is obtained. By delaying chopper pickoffs and the addition of timing circuitry, this interval can be changed as desired. The sampling rate is constrained by the desire for independent samples. A sampling rate of 50kHz has been proposed with a word length of 16 bits. Since the averaging is software controlled, the averaging period can be adjusted in flight to suit the conditions being measured to achieve the desired signal-to-noise ratio. In addition, other instrument functions, such as balancing and gain adjustment, can be performed by software controlled processing.

Sampling and quantization of the A/D is performed by scaling double precision numbers and converting to long integers then using a bitwise masking (AND) operation.

CHAPTER THREE

ANALYTICAL MODEL

3.1 Introduction

The objective of this thesis is to evaluate a digital processing approach to gas filter radiometry based on the TRACER measurement process. The purpose is to optimize radiance measurements with respect to selected model parameters. In the previous chapters the justification for atmospheric research, as well as the details of TRACER and the GFCR process were presented. This chapter describes the analytical and simulation models and gives details on the major components of the models with emphasis on the preamplifier response function. A theoretical model of the system is presented which includes the expected resolution of the differential measurement. The Gaussian noise generator is also evaluated. Validation of the model includes a piecewise evaluation of each subsystem. Figure 3.1 shows an analytic block diagram of the modeling process. The rest of this chapter describes each block in detail.

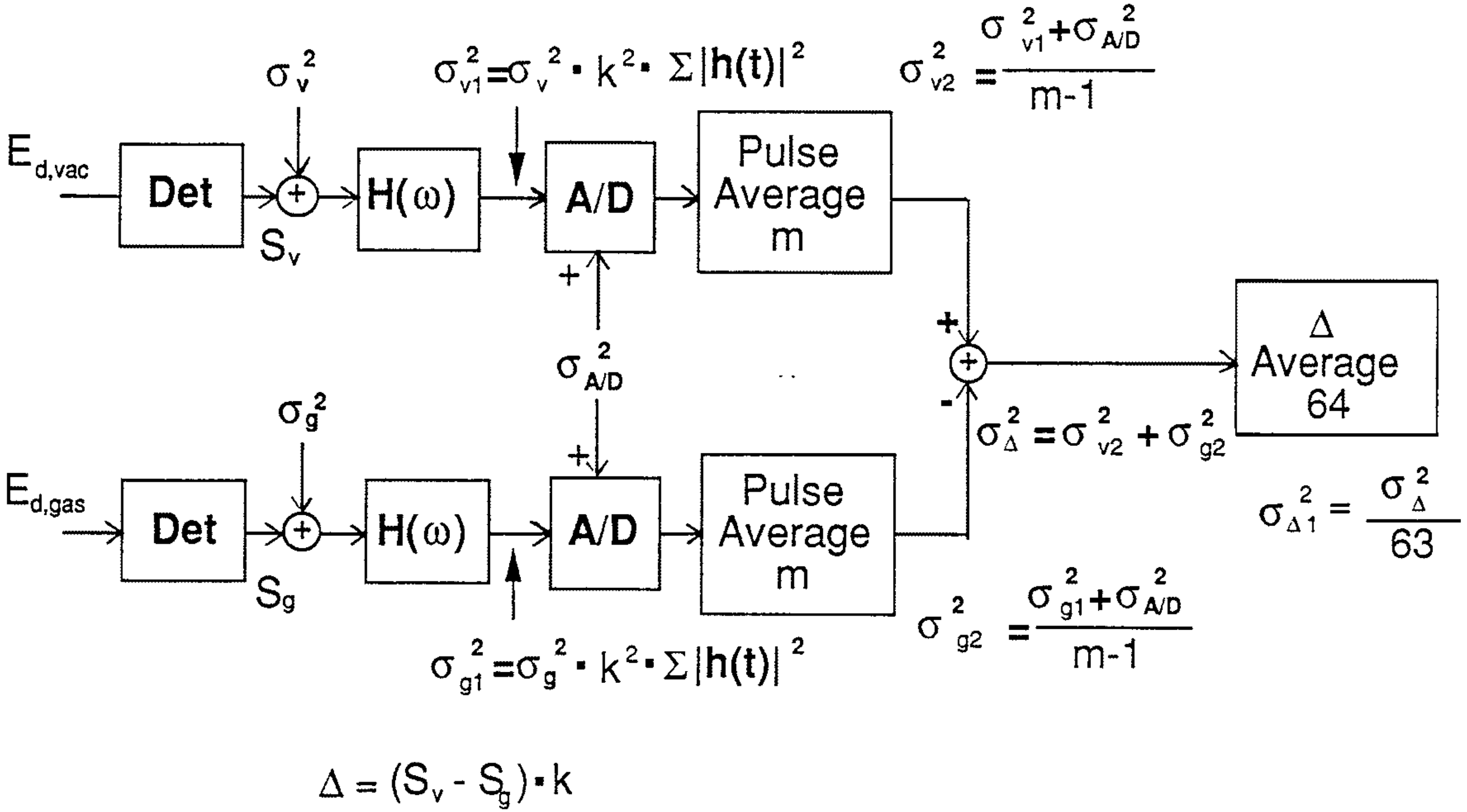

Figure 3.1. Analytical Block Diagram.

3.2 Input Signal

The desired measurement is the estimate of mean radiation power during a specified interval. This interval can be considered either spatial or temporal depending whether reference is made to the Earth target or an electronic signal. This analysis considers a time interval. The input to the model is the power incident on the detector for each gas cell, vacuum cell, and the spokes. The incident power values onto the detector used in this investigation have been previously determined and were tabulated in Table 2.1 in Chapter Two. They are assumed to be constant during a cell view and over 64 cycles. This assumption simplifies the analysis for the measurement over 64 wheel revolutions.

The normalized chopper waveform is convolved with the input signal before it reaches the detector module. The waveform shape is incorporated into the simulation process to examine the effect of system transient response on the waveform. For the 4.67μm channel radiance values, the waveform at the output of the chopper is shown in Figure 3.2. Each pulse is approximately 4.44msec and is generated with 1333 points per pulse providing a simulation base frequency, F_b, of 299925Hz.

3.3 Detector Module

Through the chopper, the input radiance is split and focused onto the detectors. In the detector/preamplifier module the radiance is converted into a current signal, noise is added, and then the signal passes through the

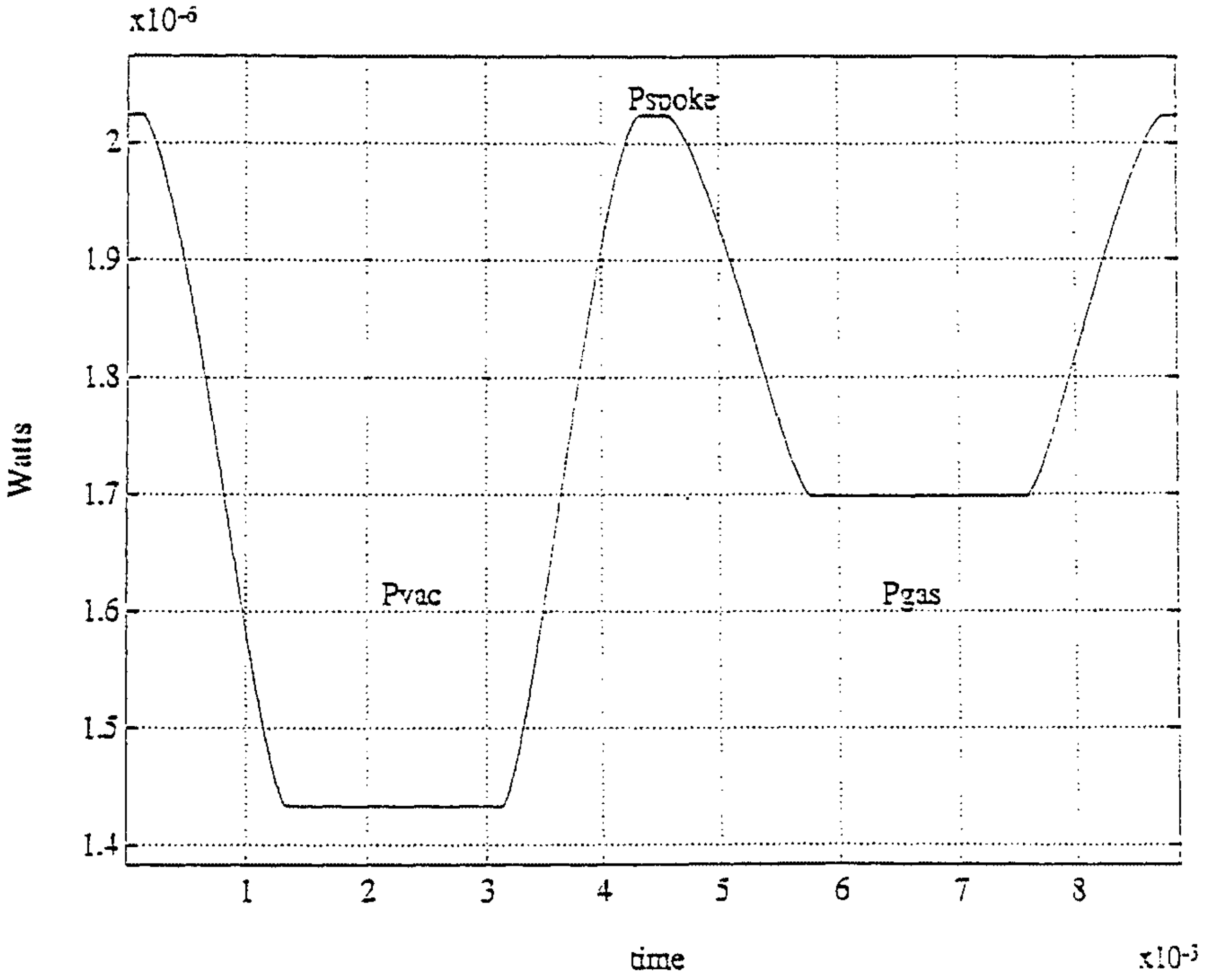

Figure 3.2. Two Pulses from Output of Chopper.

transimpedance amplifier. The transimpedance amplifier converts the current signal into a voltage signal. The effects of the preamplifier filter on the signal are discussed in section 3.4. Evaluation of the detector/preamplifier module includes testing the Gaussian number generator. These results are presented in section 3.3.1. It is noted here that the estimated detector response time, approximately 30μs, is neglected.

The input radiance, E_e, falls next onto the PV detector where the light is converted into a current signal by the equation

$$I_p = -\ .804 \cdot E_e \eta \lambda \qquad (A).$$

The negative sign is inconsequential and is dropped from the calculations. The current, I_p, produced from amplifier is assumed to be constant for a cell view since the input radiation power was assumed constant during the cell view. The expected differential current signal between a vacuum cell pulse and an adjacent gas cell pulse, designated Δ_A, is defined as

$$\Delta_A = I_{p,vac} - I_{p,gas} \qquad (A).$$

The subscript is to denote the units of Δ since the signal units go through the transformations from watts, to amps, to voltage. The incident powers given in Chapter Two produce the currents at the output of the detectors listed in Table 3.1.

Next the noise is added to the current signal. From the equations in Chapter Two, the variance of the additive noise for both the gas and evacuated cell views on the 2.33μm and 4.67μm channels are tabulated in Table 3.2. The signal value to be measured is represented as

$$S(t) = I + N(t)$$

Table 3.1. Expected Detector Output Values.

	$I_{p,vac}$ (A)	$I_{p,gas}$ (A)	Δ_A (A)	spoke(A)
4.67μm channel:	$3.767 \cdot 10^{-6}$	$4.462 \cdot 10^{-6}$	$-6.947 \cdot 10^{-7}$	$5.319 \cdot 10^{-6}$
2.33μm channel:	$4.849 \cdot 10^{-8}$	$4.836 \cdot 10^{-8}$	$1.338 \cdot 10^{-10}$	$8.591 \cdot 10^{-9}$

Table 3.2. Noise Variances.

	σ_{vac}^2	σ_{gas}^2
4.67μm channel:	$1.650 \cdot 10^{-20}$	$1.951 \cdot 10^{-20}$
2.33μm channel:	$4.162 \cdot 10^{-22}$	$4.156 \cdot 10^{-22}$

where I is the constant signal value since it is assumed that the incident radiation creates a constant signal and N(t) is the additive noise.

3.3.1 Gaussian Number Generator

The detectors/preamplifier module introduces additive noise to the signal. The noise source is modeled as a spectrally white, zero mean, Gaussian noise process. The standard deviation of the noise is the rms value of the noise. The program to generate the gaussian noise is given below [8]. Normally distributed numbers are generated by computing the following polynomial equations:

$$t = \mathrm{sqrt}(-2 \cdot \mathrm{Ln}(\mathrm{seed}))$$

$$p = p_0 + t\,(p_1 + t\,(p_2 + t\,(p_3 + t \cdot p_4)))$$

$$q = q_0 + t\,(q_1 + t\,(q_2 + t\,(q_3 + t \cdot q_4)))$$

where the p_n's and q_n's are constants, then

$$\text{Normal} = (p\,/\,q) - t.$$

To evaluate the gaussian number generator, three tests were performed [9]. These are the interval test for the mean, interval test for the variance, and the chi-square goodness-of-fit test for the distribution. The interval tests express how close the calculated mean or variance is to the true value with a certain confidence. The goodness-of-fit test relates with a significance level how well the distribution fits the theoretical Gaussian distribution. For these tests a normal distribution, $N(\mu,\sigma^2)$, with mean, $\mu=0$, and standard deviation, $\sigma=1$, is used as a test input.

To test the mean, the following theorem is used [9].

Theorem: If $(x_1, \ldots, x_n)$ is a random sample of size n from $N(\mu,\sigma^2)$, then m is an $N(\mu,\sigma^2/n)$ random variable where

$$m=\frac{1}{n}\sum_{1}^{n} x_i$$

is the sample mean. A $(1-\alpha)\cdot 100\%$ confidence interval for μ is

$$[m \pm z_{\alpha/2}\cdot\sigma/\sqrt{n}].$$

This means that the probability is $1-\alpha$ that $[m \pm z_{\alpha/2}\cdot\sigma/\sqrt{n}]$ contains μ.

To test the variance, the following theorem is used [9].

Theorem: If $(x_1, \ldots, x_n)$ is a random sample of size n from $N(\mu,\sigma^2)$, where

$$s^2=\frac{1}{n-1}\sum_{1}^{n}(x_r-m)^2$$

is the sample variance, and m is the sample mean, then

$$(n-1)\frac{s^2}{\sigma^2}$$

has the chi-square distribution with n-1 degrees of freedom. This means that we can write:

$$P[\chi_{n-1,1-\frac{\alpha}{2}}\leq(n-1)\frac{s^2}{\sigma^2}\leq\chi_{n-1,\frac{\alpha}{2}}]=1-\alpha$$

or

$$P[\frac{(n-1)s^2}{\chi_{n-1,1-\frac{\alpha}{2}}}\leq\sigma^2\leq\frac{(n-1)s^2}{\chi_{n-1,\frac{\alpha}{2}}}]=1-\alpha$$

This is called a $(1-\alpha)\cdot 100\%$ confidence interval for σ^2.

The chi-square goodness-of-fit test is given below [9]. To test the hypothesis that our sample comes from a normal population with probabilities Θ_i $i=1, \ldots k$ where Θ_i are known, we use the test statistic:

$$\chi^2=\sum_{1}^{k}\frac{(f_r-n\theta_i)^2}{n\theta_i}$$

where n is the number of points, Θ_i are the theoretical frequencies, k is the number of intervals, and f_i are the observed frequencies. For moderately large values of n, the test statistic is approximately the chi-square distribution with l degrees of freedom, usually $l = k-1$. Testing at the $\alpha\cdot 100\%$ level of significance, the observed value of χ^2 is considered significant at this level if $\chi^2 > \chi^2_{l,\alpha}$. ie. large χ^2 means poor fit and the hypothesis is rejected. A significance level of 5% is used, corresponding to a 95% confidence level. The probability that a random sample produces a χ^2 value greater than some specified value is equal to the area under the chi-square density curve to the right of this value. This test is commonly called the chi-square goodness-of-fit test. Also note the requirement that $n\Theta_i > 5$ for all i which may decrease the number of degrees of freedom.

These tests were run with μ=0 and σ^2=1 at a 95% confidence level, N is the number of points, and k is the number of bins ($k \approx \sqrt{N}$). All tests were performed 10 times with N = 8192, 401, and 64. Results for the mean and variance tests represent the number of times, out of 100, that the sample mean or variance fell within calculated intervals. Results.of the chi-square test shows the chi-square test statistic for one sequence of length N. The results of these tests are shown in Table 3.3.

Summarizing these results at the 95% level of confidence, it is seen that both the mean and variance are within the calculated intervals for more than 93% of the trials for sequences of length 64, 401, and 8192 points. At the 95% confidence level the results of the chi-square tests show that the hypothesis that the sample came from a normal distribution would be accepted. All but one of the χ^2 test statistics are greater than their respective $\chi^2_{l,.05}$ values. A visual assessment of the histograms also showed good correlation between data sequences and values computed from a normal distribution.

Test 1. N = 8192; k = 90; l = 69; $\chi^2_{l,.05} = 89.391$

i	% mean	% var	χ^2
1	98/100	97/100	63.151
2	93/100	94/100	45.754
3	97/100	96/100	65.265
4	92/100	99/100	77.019
5	91/100	96/100	69.459
6	95/100	96/100	72.747
7	94/100	95/100	63.050
8	91/100	94/100	91.494
9	91/100	96/100	69.681
10	96/100	97/100	59.894
avg=	93.8%	96.0%	

Test 2. N = 401; k = 20; l = 18; $\chi^2_{l,.05} = 28.869$

i	% mean	% var	χ^2
1	97/100	95/100	13.705
2	93/100	96/100	11.399
3	98/100	98/100	10.521
4	93/100	92/100	18.040
5	94/100	96/100	13.359
6	96/100	97/100	5.363
7	92/100	100/100	11.710
8	96/100	93/100	11.978
9	95/100	97/100	17.510
10	98/100	94/100	14.835
avg=	95.2%	95.8%	

Test 3. N = 64; k = 8; l = 7; $\chi^2_{l,.05} = 14.067$

i	% mean	% var	χ^2
1	98/100	96/100	2.908
2	95/100	97/100	4.151
3	94/100	97/100	7.897
4	96/100	92/100	1.052
5	94/100	90/100	9.668
6	97/100	93/100	2.996
7	99/100	91/100	2.461
8	96/100	94/100	3.083
9	97/100	91/100	3.657
10	97/100	93/100	6.893
avg=	96.3%	93.4%	

Table 3.3. Results of Random Number Generator Tests.

3.4 Preamplifier Module

The transimpedance amplifiers filter the input signal and convert the current signals into voltages. This conversion from current to voltage has been modeled as a 1:1 transformation. A gain factor, k, of the amplifiers is incorporated as one lump sum. The gain is determined for each channel such that the largest input signal produces a 7 volt output. The transfer function of the noise through the filter is described by application of the response of the filter to random signals. Since independent samples are desired, the criterion for independent samples is explained in section 3.5.

3.4.1 Response of Filter to Random Signals

The frequency response of the preamplifiers is modeled as a digital two pole Butterworth invariant impulse lowpass linear filter to represent the amplifier's high frequency rolloff. They are the main spectral shapers in the system. It is necessary to determine the variance of the noise at the output of the filter with transfer function H(ω), designated σ_y^2, given that the variance of the noise at the input is σ_x^2.

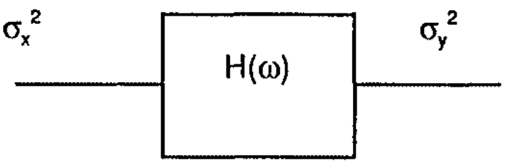

It is assumed that the additive input noise is not spectrally shaped since the preamplifier cutoff frequency, F_c, will be much smaller than the simulation base frequency, F_b, such that the input noise will appear white over the frequency range of interest. For a wide sense stationary process, the variance does not depend on time and is given by [10]:

$$\sigma^2 = R(0)-\mu^2$$

where μ is the mean and $R(\tau)$ is the autocorrelation function of the noise. Since the input noise is assumed to have zero mean,

$$\sigma_x^2 = R_x(0).$$

The variance of the noise at the output of the filter can be written

$$\sigma_y^2 = R_y(0)-\mu_y^2.$$

The mean of the output is related to the mean of the input by [11]

$$\mu_y = \mu_x \int h(t)dt.$$

Thus, the mean of the output is the mean of the input process times the area under the impulse response, which is the dc gain. But since the mean of the additive noise is zero, $\mu_x = 0$, then $\mu_y = 0$ so that

$$\sigma_y^2 = R_y(0).$$

The power spectral density, $S(\omega)$ is the Fourier transform of the autocorrelation [10] where

$$R_y(\tau) = 1/(2\cdot\pi) \int S_y(\omega)e^{j\omega\tau}d\omega.$$

At $\tau = 0$,

$$R_y(0) = 1/(2\cdot\pi) \int S_y(\omega)d\omega.$$

The power spectral density of the response of a linear time-invariant system with transfer function $H(\omega)$ is [10]

$$S_y(\omega) = S_x(\omega) \left| H(\omega) \right|^2,$$

this can be substituted into the above equation to get

$$R_y(0) = 1/(2\cdot\pi) \int S_x(\omega) \,|\, H(\omega) \,|^2 d\omega = \sigma_y^2.$$

The spectral density of the zero mean input must be determined. The variance is:

$$\sigma_x^2 = R_x(0).$$

Using the inverse Fourier transform at τ=0:

$$S_x(\omega) = \int R_x(\tau) d\tau.$$

The limits of the integral become 0 since theoretically, the function is only defined for R(0). Thus, the spectral density of the input is the variance:

$$S_x(\omega) = \sigma_x^2.$$

and

$$\sigma_y^2 = 1/(2\cdot\pi)\cdot\sigma_x^2 \int |\, H(\omega) \,|^2 d\omega.$$

Using Parsevals theorem given below [12]

$$\int |\, f(t) \,|^2 dt = 1/(2\cdot\pi) \int |\, F(\omega) \,|^2 d\omega,$$

the following can be obtained:

$$\int |\, H(\omega) \,|^2 d\omega = 2\cdot\pi \int |\, f(t) \,|^2 dt.$$

The variance of the output process can also be written:

$$\sigma_y^2 = \sigma_x^2 \int |\, h(t) \,|^2 dt.$$

The equation $\int | h(t) |^2 dt$ can be estimated by $\Sigma | h(t) |^2$ where h(t) is empirically found by forcing an impulse on the filter. The normalized values of $\Sigma | h(t) |^2$ are tabulated in Table 3.4 for the three selected cutoff frequencies and is plotted versus frequency in Figure 3.3. Also plotted on this graph is s_o^2/s_i^2 where s_o^2 is the sample variance calculated at the output of the filter and s_i^2 is the sample

Table 3.4. Normalized Values of $\Sigma|h(t)|^2$ for Each Cutoff Frequency.

F_c	$\Sigma\|h(t)\|^2$
2k	.0148176
4k	.0296613
10k	.0748178

variance calculated at the input. It is noted that $\Sigma|h(t)|^2$ closely approximates calculated values of output to input sample variance.

In deriving the equation for the variance of the noise at the output of the filter, the gain factor was assumed to be unity. For a gain factor, k, the equation becomes:

$$\sigma_y^2 = \sigma_x^2 \cdot k^2 \, \Sigma|h(t)|^2.$$

The gain was selected such that the maximum quantity seen by the A/D would be seven volts. The gain is held constant at $k_{4.67} = 1.28 \cdot 10^6$ and $k_{2.33} = 145 \cdot 10^6$. The expected signal in Table 3.5. Expected noise values at the output of the amplifier are tabulated in Table 3.6. As shown in Table 3.6, smaller cutoff frequencies attenuate the signal variance more than larger cutoff frequencies.

Table 3.5. Expected Signal Values at the Output of the Amplifier Module.

	$V_{p,vac}$ (A)	$V_{p,gas}$ (A)	Δ_V (V)	spoke(V)
4.67μm channel:				
	4.822	5.711	-0.889	6.808
2.33μm channel:				
	7.031	7.011	0.019	1.246

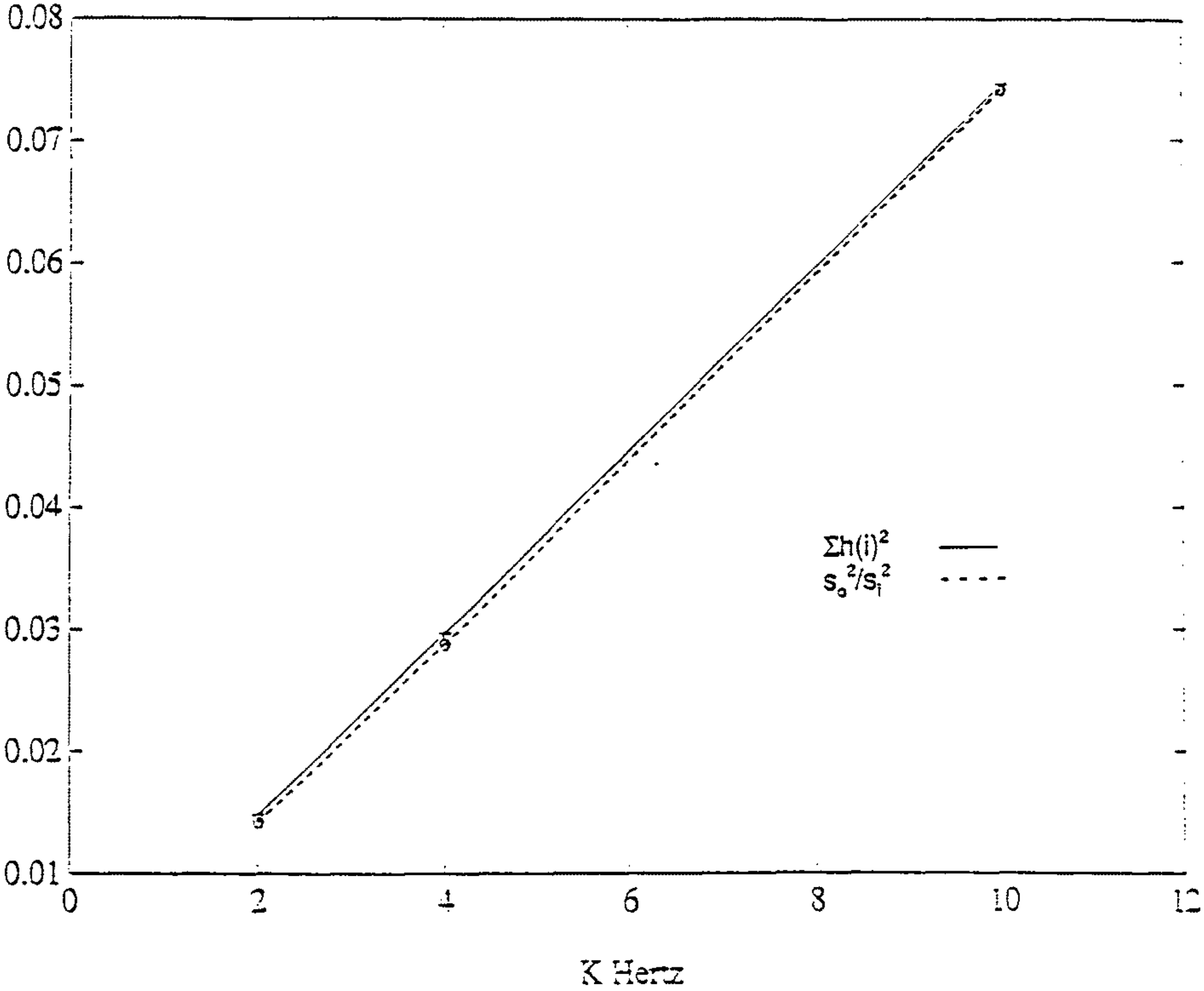

Figure 3.3. $\Sigma h(i)^2$ verses s_o^2/s_i^2.

Table 3.6. Expected Noise Values at Amplifier Output.

$F_c = 2\text{kHz}$	σ_{vac}^2	σ_{gas}^2
4.67μm channel:	$4.006\cdot10^{-10}$	$4.736\cdot10^{-10}$
2.33μm channel:	$1.297\cdot10^{-07}$	$1.295\cdot10^{-07}$
$F_c = 4\text{kHz}$	σ_{vac}^2	σ_{gas}^2
4.67μm channel:	$8.019\cdot10^{-10}$	$9.481\cdot10^{-10}$
2.33μm channel:	$2.596\cdot10^{-07}$	$2.592\cdot10^{-07}$
$F_c = 10\text{kHz}$	σ_{vac}^2	σ_{gas}^2
4.67μm channel:	$2.023\cdot10^{-09}$	$2.392\cdot10^{-09}$
2.33μm channel:	$6.547\cdot10^{-07}$	$6.538\cdot10^{-07}$

3.5 Independent Samples Criterion

The output sequence becomes highly correlated due to the filtering process. Independent samples are desired for the averaging process so that by averaging, the variance of the estimate is reduced by $1/(n-1)^{1/2}$ if the n samples are independent [13]. If the random variables x_i are independent, they are also uncorrelated [13]. For Gaussian noise, uncorrelated samples are independent.

The independence of samples at the output of the filter is investigated by considering the autocorrelation of these samples. The autocorrelation is a measure of the dependence between values of the random process at different times. To determine the correlation of the output sequence the spectrum of the filtered signal is estimated. For an ideal lowpass filter with power spectrum, $S(\omega)$, the autocorrelation is the sinc function, $(\sin x)/x$. This is graphically presented in Figure 3.4. The samples are uncorrelated where the autocorrelation is zero, or at $t = n/(2 \cdot F_c)$, $n = 1,2,3...$. For the ideal filter, the greatest independence between samples and the lowest sampling rate occurs at $t = 1/(2 \cdot F_c)$ or equivalently, $F_{samp} = 2 \cdot F_c$.

The filter used for the simulations is not ideal, ie. it is has some transition band, and therefore the autocorrelation function of the output sequence will have a larger main lobe and smaller side lobes than the ideal case. Since the input noise was assumed white over the frequency range of interest, the output spectrum is windowed by the frequency response of the filter. The autocorrelation of the output sequence was computed with

$$\mathrm{FFT}^{-1}[|h(f)^2|]$$

where $h(f)$ is the frequency response of the filter.

The frequency response was obtained by taking the FFT of the filter impulse response and the impulse response was empirically obtained by passing an impulse through the filter. The autocorrelation at the output of each of the three filters, F_c= 2k, 4k, and 10k as computed above is shown in Figures 3.5a,b,c.

The zero autocorrelation sampling rates for each cutoff frequency is shown in Table 3.7. Therefore, for each cutoff frequency, the number of independent

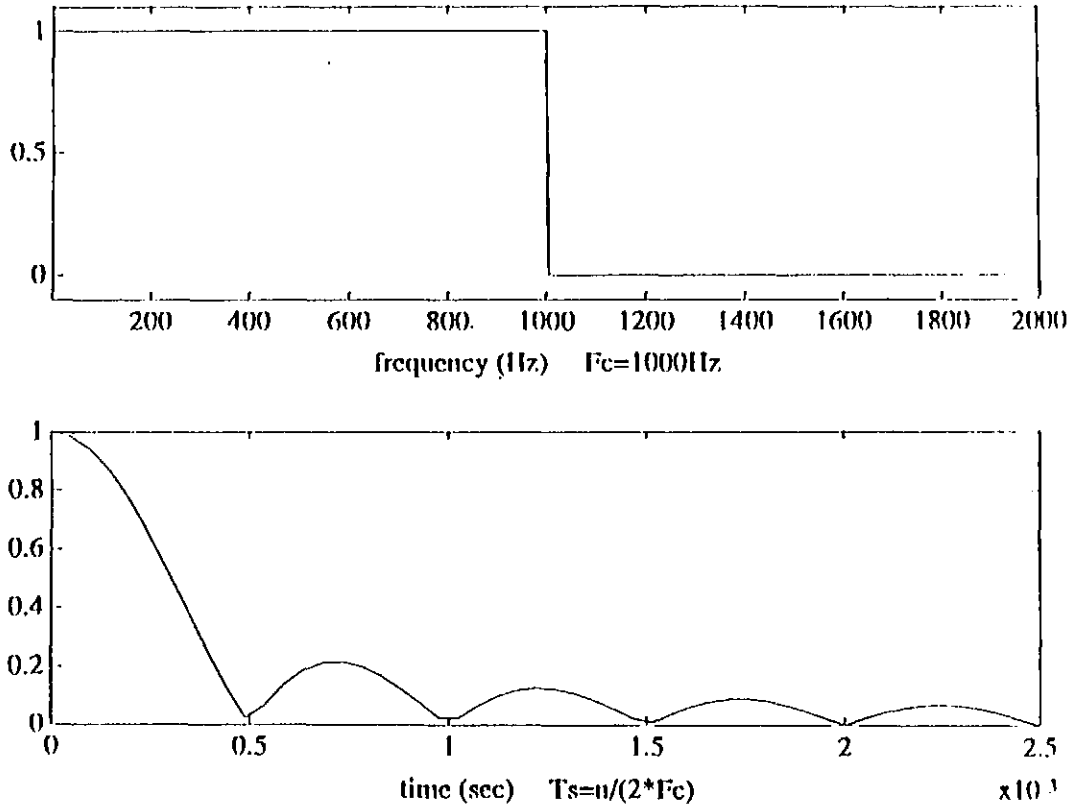

Figure 3.4. Ideal Lowpass Filter and its Autocorrelation.

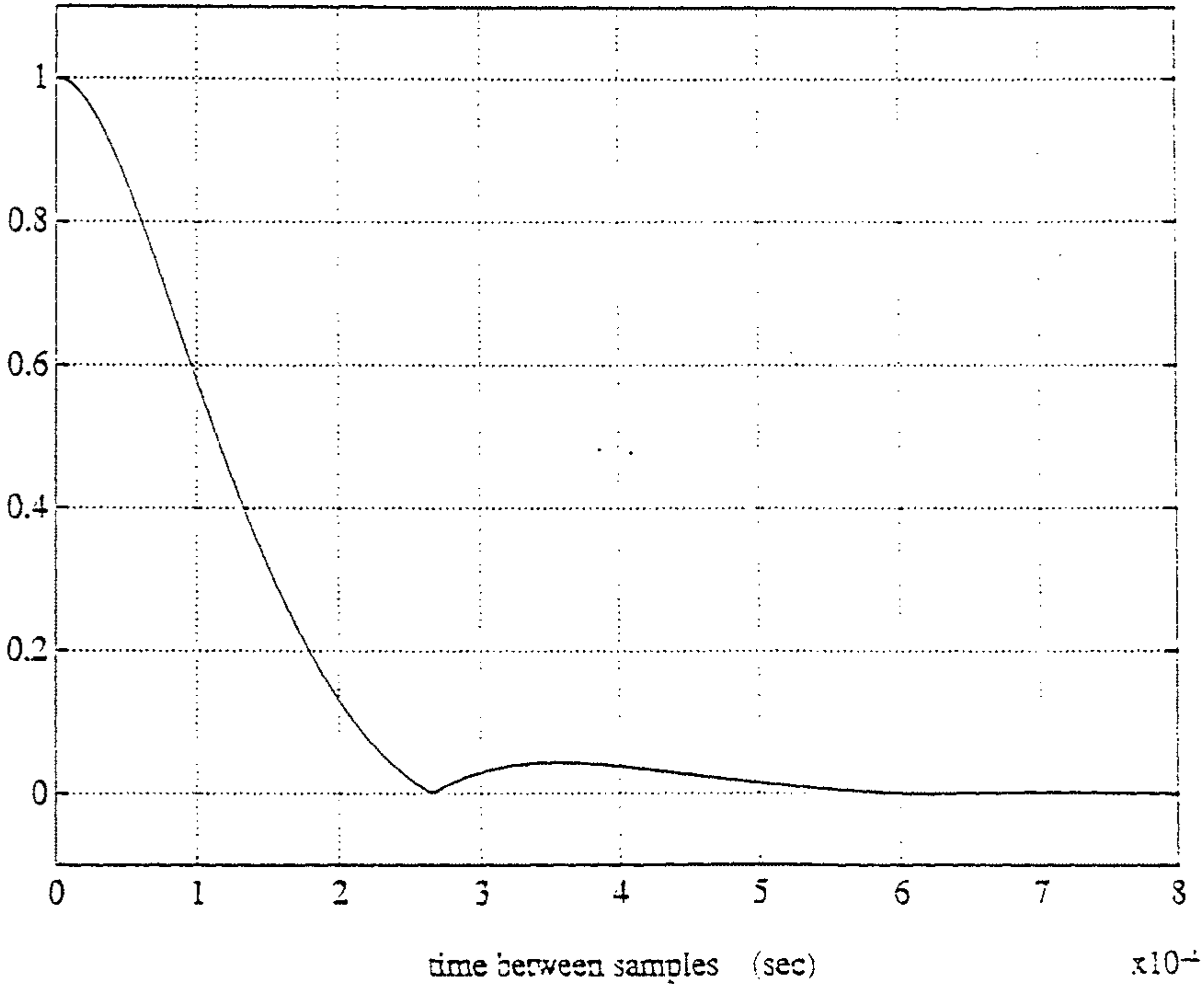

Figure 3.5a. Autocorrelation of Filter Response at F_c=2k.

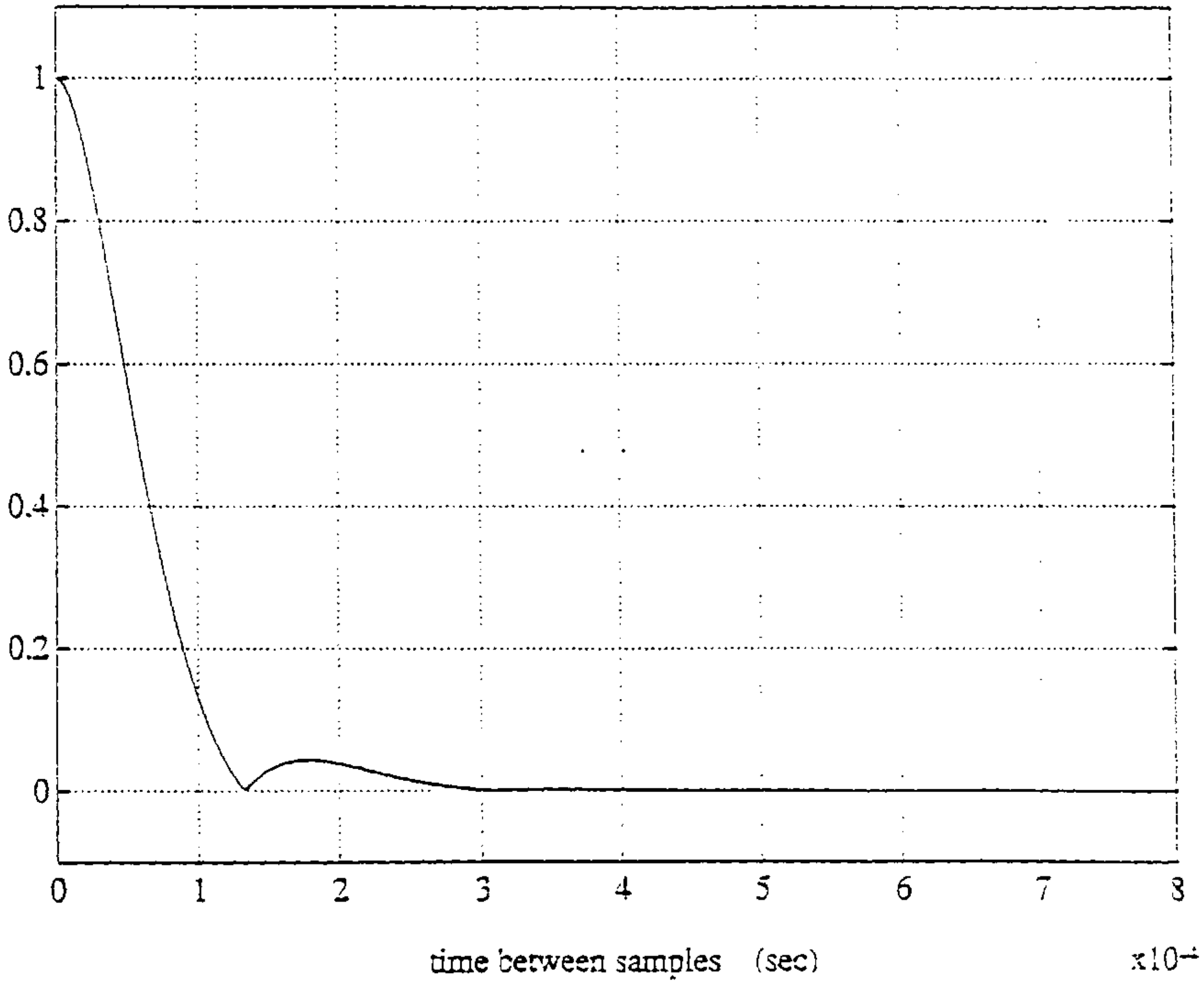

Figure 3.5b. Autocorrelation of Filter Response at F_s=4k.

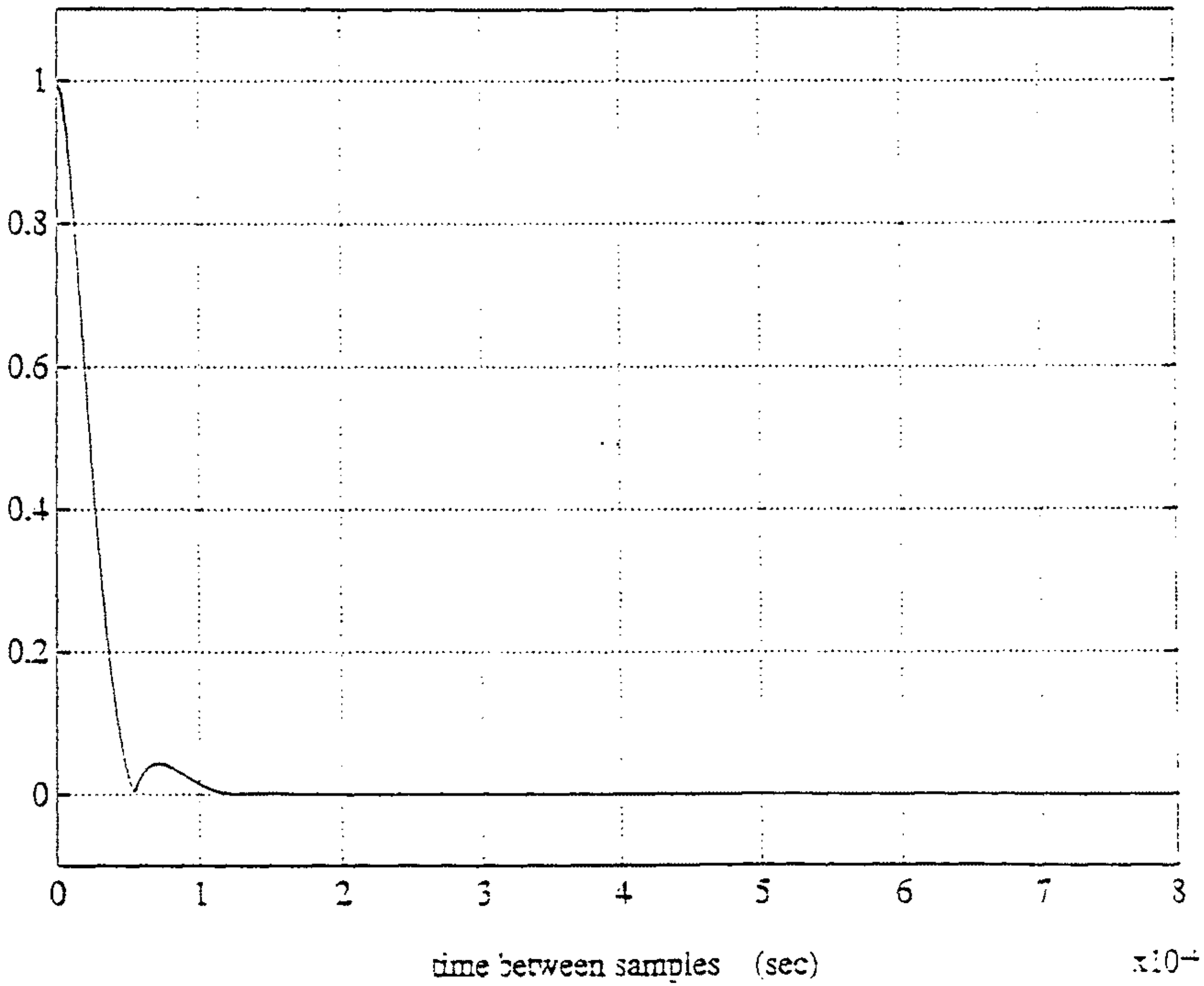

Figure 3.5c. Autocorrelation of Filter Response at F_c=10k.

Table 3.7. Zero autocorrelation sampling frequency for each cutoff.

F_c (Hz)	$F_{s,\ \mathrm{zero\ autocorrelation}}$ (Hz)
2k	3749
4k	7315
10k	17643

samples per pulse is fixed. It is noted that the zero autocorrelation sampling frequency is slightly less than twice the filter cutoff frequency, as was the case with the ideal filter.

3.6 Sampling and Quantization

The amplifier cutoff frequency and the quantization length determine the window during which samples are taken. The cutoff frequency determines where the pulse is maximally flat and filter transient effects are negligible and the quantization length is considered to limit measurement bias. Given the sampling frequency and the sampling window, the number of independent sample points per pulse is established.

Quantization of the samples also introduces noise. For a complex signal, the equation for the variance of two's complement truncated numbers is given below.

$$\sigma_{A/D}^2 = (10/2^b)^2/12$$

where b is the quantization bit length, and 10 is the peak to peak range. Since the magnitude of the signal at the A/D is limited to 7 V by selection of gain, clipping is eliminated. The variance for truncation of two's complement numbers for each quantization length is calculated in Table 3.8. The expected noise variances at the

Table 3.8. Quantization Noise Variance.

b	$\sigma_{A/D}^2$
16	$1.94 \cdot 10^{-9}$
12	$4.97 \cdot 10^{-7}$
10	$7.95 \cdot 10^{-6}$
8	$1.27 \cdot 10^{-4}$

input to the A/D module given in Table 3.6 are compared with the theoretical variances due to truncation in Table 3.8. It is seen that on the 4.67μm channel, the quantization noise becomes significant for quantization lengths less than 16 bits. On the 2.33μm channel, the quantization length becomes significant at 12 bits.

The amplifier cutoff frequency and the quantization length determine the window during which samples are taken. The cutoff frequency determines where the pulse is maximally flat and filter transient effects are negligible. The quantization length is considered since the measurement error is constrained by it. Given the sampling frequency and the sampling window, the number of independent sample points per pulse is established.

Since the quantization length can potentially add a bias to the measurement, the sampling window had to be carefully selected. To determine this window, a normalized chopper waveform was filtered at each cutoff frequency, at the three selected sampling rates, and then quantized at each quantization length. For a chopper waveform of 1333 equally spaced points, the 'flat top' of the unfiltered waveform is bounded by the points between 421 and 930. Since filtering the waveform introduces ripple on the beginning of the 'flat top', the last sample point was fixed at 930 and the starting point was varied. Samples from the windows were averaged and the absolute error between the window averages and 1, the normalized 'flat top' value, was computed. These results are shown in Tables 3.9a,b,c. From these results, the optimal sampling window and the number of samples taken during this interval for each case was determined.

From the results presented in Tables 3.9a,b,c, it is observed that there will be some inherent measurement bias due to sample quantization since none of the errors are zero. The magnitude of the errors decreases by about an order of magnitude as selected the quantization lengths increase. The lowest errors for each sampling frequency, cutoff frequency and quantization length are marked with an asterisk (*). The larger number of samples was chosen if the error was the same. The number of samples taken for each case is summarized in Table 3.10.

3.7 Resolution of Δ

One major issue is to determine the resolution with which the difference measurement can be calculated. The difference measurement is the difference between average values of vacuum and gas filled cells over 64 chopper revolutions. The output variance is the measurement noise. Both point estimates and interval estimates are considered.

F_c = "Zero" Autocorrelation sampling

Fc=2000 Fsamp=3749 Tend=930
number of (simulation) points between samples (Fb/Fsamp) = 80

Nsamp	Tstart	qlen=8	qlen=10	qlen=12	qlen=16
4	690	.017547	---	.000458	.000114
5	610	" "	.007782	" "*	.000061*
6	530	" "	" "*	.000865	.000229
7	450	" "	.009177	.002202	.001460
8	370	-.016632*	-.023956	-.030365	-.031128
9	290	-.099640	---	---	---

%%

Fc=4000 Fsamp=7315 Tend=930
number of (simulation) points between samples (Fb/Fsamp) = 41

Nsamp	Tstart	qlen=8	qlen=10	qlen=12	qlen=16
11	520	.017547	---	.000458	.000125
12	479	" "	.007782	" "*	.000102*
13	438	" "	" "	.000833	.000375
14	397	.014757	-.004992*	-.001984	-.002442
15	356	.000682*	-.011098	-.017772	---
16	315	-.031281	-.041657	-.047913	---

%%

Fc=10000 Fsamp=17643 Tend=930
number of (simulation) points between samples (Fb/Fsamp) = 17

Nsamp	Tstart	qlen=8	qlen=10	qlen=12	qlen=16
30	437	.017547	.007782	---	.000147
31	420	" "	" "	.000458	.000152
32	403	" "	" "	" "*	.000129*
33	386	.016364	.006598	-.000726	-.001101
34	369	.012952	.003186	-.003990	-.004412
35	352	.007503	-.002542*	-.009657	-.010113
36	335	-.000899*	-.010936	---	-.018306
37	318	-.012013	-.021779	---	---

Table 3.9a. Number of sample points and measurement error with respect to qlen, F_c, and F_s at the zero autocorrelation sampling frequency.

F_c = Twice "Zero" Autocorrelation sampling

Fc=2000 Fsamp=7498 Tend=930
number of (simulation) points between samples (Fb/Fsamp) = 40

Nsamp	Tstart	qlen=8	qlen=10	qlen=12	qlen=16
7	690	.017547	---	.000458	.000109
9	610	" "	.007782	" "*	.000068*
11	530	" "	" "*	.000680	.000111
13	450	" "	-.008533	.001980	.001373
15	370	-.005890*	-.013703	---	---
17	290	-.078960	---	---	---

%%

Fc=4000 Fsamp=14630 (14282) Tend=930
number of (simulation) points between samples (Fb/Fsamp) = 21

Nsamp	Tstart	qlen=8	qlen=10	qlen=12	qlen=16
20	520	.017547	---	.000458	.000137
22	479	" "	.007782	" "*	.000118*
24	437	" "	" "	.000763	.000299
26	395	.016045	-.005904*	-.001045	-.001503
28	353	.000806*	-.008610	---	---
30	311	-.028025	-.038117	---	---

%%

Fc=10000 Fsamp=35286 (37490) Tend=930
number of (simulation) points between samples (Fb/Fsamp) = 8

Nsamp	Tstart	qlen=8	qlen=10	qlen=12	qlen=16
62	437	---	---	---	.000148
64	420	---	---	.000458	" "
66	403	---	.007782	.000495*	.000150*
68	386	---	.006933	-.000285	-.000670
70	369	.014246	.003931	-.003015	-.003430
73	352	.009521	-.001181*	-.008071	---
75	335	-.001402*	-.009145	---	---
76	319	-.007818	-.018725	---	---

Table 3.9b. Number of sample points and measurement error with respect to qlen, F_c, and F_s at twice the zero autocorrelation sampling frequency.

F_s = "Analog" sampling frequency = F_b = 299925

Fc=2000 Tend=930
number of (simulation) points between samples (Fb/Fsamp) = 1

Nsamp	Tstart	qlen=8	qlen=10	qlen=12	qlen=16
241	690	.017547	.007782	.000458	.000105
321	610	" "	" "	" "	.000094
401	530	" "	" "	.000500*	.000046*
481	450	" "	.008594	.001823	.001243
561	370	.005501*	-.004195*	-.010505	-.011158
641	290	-.058018	-.068302	-.074282	-.074995

%%%

Fc=4000 Tend=930
number of (simulation) points between samples (Fb/Fsamp) = 1

Nsamp	Tstart	qlen=8	qlen=10	qlen=12	qlen=16
411	520	.017547	.007782	.000458	.000143
452	479	" "	" "	" "	.000125*
493	438	" "	" "	.000601	.000214
534	397	.017108	.007087	.000188*	-.000250
575	356	.007765*	-.002629*	-.009278	-.009762
616	315	-.016125	-.026810	-.033270	-.033794

%%%

Fc=10000 Tend=930
number of (simulation) points between samples (Fb/Fsamp) = 1

Nsamp	Tstart	qlen=8	qlen=10	qlen=12	qlen=16
494	437	.017547	.007782	.000458	.000149
511	420	" "	" "	" "	.000147*
528	403	" "	" "	.000513	.000164
545	386	.017117	.007155	-.000004*	-.000385
562	369	.014906	.004741	-.002310	-.002716
579	352	.010329	.000040*	-.006913	-.007341
596	335	-.003259*	-.007162	-.014011	-.014454
613	318	-.006349	-.016863	-.023638	-.024098

Table 3.9c. Number of sample points and measurement error with respect to qlen, F_c, and F_s at the 'analog' sampling frequency.

Table 3.10. Number of Sample Points Used for Each Case.

$F_{s,\text{zero autocorrelation}}$					
	F_c	qlen=8	qlen=10	qlen=12	qlen=16
	2000	8	6	5	5
	4000	15	14	12	12
	10000	36	35	32	32
$F_{s,2\text{'zero autocorrelation}}$					
	F_c	qlen=8	qlen=10	qlen=12	qlen=16
	2000	15	11	9	9
	4000	28	26	22	22
	10000	75	73	66	66
$F_{s,\text{'analog' frequency}}$					
	F_c	qlen=8	qlen=10	qlen=12	qlen=16
	2000	561	561	401	401
	4000	575	575	534	452
	10000	596	579	545	511

The sample mean and sample variance are used to estimate signal values. They are both unbiased estimators. It is assumed that each sample as well as each pulse is statistically independent. The following analysis, i represents a sample of either a gas or vacuum cell pulse, j represents a pulse pair and k represents an experiment number. One experiment consists of a set of 64 pulse pairs. For a gas cell view the sample mean is

$$G_j = 1/m \cdot \Sigma g_i \qquad i = 1 \text{ to } m$$

where g_i represents a sample from a gas cell view. Similarly, the sample mean for a vacuum cell is

$$V_j = 1/m \cdot \Sigma v_i \qquad i = 1 \text{ to } m$$

where v_i represents a sample from a vacuum cell view. For one pulse pair, the difference between a vacuum cell view and a gas cell view, designated

$$D_j = V_j - G_j.$$

For one experiment, the sample mean of the D_j's, designated $sm(D_k)$, is

$$sm(D_k) = 1/64 \cdot \Sigma D_j \quad j = 1 \text{ to } 64.$$

For one experiment, the sample variance of the D_j's, designated $sv(D_k)$, is

$$sv(D_k) = 1/63 \cdot \Sigma(D_j - sm(D_k))^2 \quad j = 1 \text{ to } 64.$$

The variance of the difference measurement, $sv(D_k)$, tells us about the allowable noise on the signal.

Since each experiment is conducted 50 times, the sample mean and variance of the 50 experiments can also be computed. To compute the sample statistics for this case, the means over 64 pulse pairs for both the vacuum and gas cells are computed. These are designated $\mathbf{V}_k$ and $\mathbf{G}_k$ where

$$\mathbf{V}_k = 1/64 \cdot \Sigma V_j \quad {}_{j = 1 \text{ to } 64}$$

and

$$\mathbf{G}_k = 1/64 \cdot \Sigma G_j \quad {}_{j = 1 \text{ to } 64}.$$

Then for one experiment, the differential over 64 pulse pairs is

$$\mathbf{D}_k = \mathbf{V}_k - \mathbf{G}_k.$$

The sample mean for the set of 50 experiments, designated, $sm(\mathbf{D})$, is

$$sm(\mathbf{D}) = 1/50 \cdot \Sigma \mathbf{D}_k \quad k = 1 \text{ to } 50,$$

The sample variance, designated $sv(\mathbf{D})$, is

$$sv(\mathbf{D}) = 1/49 \cdot \Sigma(\mathbf{D}_k - sm(\mathbf{D}))^2 \quad k = 1 \text{ to } 50.$$

The sample means and variances of D and **D** are compared to the theoretical values obtained in the analytical model which was presented at the beginning of this chapter. More specifically, $sm(D_k)$ and $sm(\mathbf{D})$ are compared with

Δ, sv(D_k) is compared with σ_Δ^2, and sv($\mathbf{D}$) is compared with $\sigma_{\Delta 1}^2$. Comparing the sample and theoretical variances over the 50 experiments aids in assessing the validity of the analytical model.

CHAPTER FOUR

MODEL SIMULATION

4.1 Introduction

This chapter discusses the simulation plan, presents results of the simulation, and discusses design issues the simulation will clarify. The quantity of concern is the differential output of the averaging process. The term local average will be taken to mean the pulse value averaged over 1 chopper pulse (1 chopper revolution) and the term collective average is the average of 64 pulses (64 chopper revolutions). The term 'delta' will refer to the initial reference value onto the detectors.

The purpose of this investigation is to make a performance comparison based on measurements from parameter sets to provide TRACER with useful information on the quality of the measurement. Also, it is desired to compare the empirical measurement values obtained through simulation with theoretical values obtained from the analytical model. The amplifier cutoff frequency, the A/D sampling frequency, and the A/D quantization length are the parameters which are varied for the investigation. A set of fixed instrument optical and detector parameters were defined based on the equations in Chapter Two. These fixed parameters are wavelength, quantum efficiency, preamplifier input current noise, detector temperature, detector resistance, feedback resistance, gain, and noise bandwidth. The gain was determined by the largest gas cell value for each particular channel to produce a 7 volt maximum output signal.

4.2 Simulation Plan

Three major parameters are varied for analysis. These are the preamplifier cutoff frequency, F_c, the sampling frequency, F_s, and the quantization length, qlen. The discussion below describes why these parameters were chosen as the variables.

The preamplifier cutoff frequency, F_c, dictates the response speed of the system. A smaller cutoff frequency reduces noise level at the expense of slower system response thus reducing the sampling window. The sampling windows used, as well as the noise attenuation factors for each cutoff frequency were determined in Chapter Three. The three cutoff frequencies investigated are 2kHz, 4kHz, and 10kHz.

The effect of varying the A/D sampling frequency, F_s, is also examined. This parameter governs the number of samples taken during the sampling window. It was shown in Chapter Three that these samples should be independent since for n independent samples, the variance of the measurement is reduced by a factor of $1/(n-1)^{1/2}$. F_s is tested at the frequency of zero autocorrelation, $F_{s,z}$, and at twice this frequency, $F_{s,2z}$. F_s is also tested at 299925Hz, the simulation base frequency. The latter sampling frequency will provide a comparison to the conventional analog integrate and dump process and also provide a measure of how severe oversampling influences the measurement.

The quantization length is tested at 16, 12, 10 and 8 bits. 16 bits is the design specification suggested in the TRACER proposal. It was shown in Chapter Three that a quantization length of 16 bits was desired on the 4.67µm channel and 12 bits was desired on the 2.33µm channel.

To limit the number of simulation cases, extreme values of input signal are used. Since the expected input radiance through a gas filled cell is greater on the 4.67µm channel than the 2.33µm channel, the first case corresponds to the maximum expected differential signal on the 4.67µm channel. The other case corresponds to the minimum expected differential signal value on the 2.33µm channel. The radiance through the vacuum cells is constant for each particular channel. These cases correspond to the signal and noise values presented in Chapter Three.

Each simulation is performed at all selected quantization lengths, cutoff frequencies and sampling frequencies for both 4.67µm and 2.33µm channels. Simulations are also run for both channels with ten times the calculated noise values at the "zero autocorrelation" sampling frequency. The simulation values computed are the local average of m points for a single gas and vacuum pulse, and the collective average of 64 gas and vacuum pulses. From these averages, the local and collective differential averages are computed. Each experiment is conducted 50 times.

4.3 Simulation results

To evaluate the results of the simulation trials, the differential local and collective differential averages, as well as local and collective sample variances are observed. The goal of the measurement is to determine the differential scene radiance between a gas cell view and a vacuum cell view. Assuming that the optics present no error, the difference between the presumed radiance on the detectors and the sample means represents the measurement error. This error is a random variable assumed to have zero mean and variance σ_e^2. Of interest is the effect of the simulation parameters on σ_e^2. For this study, the sample variances are compared with the theoretical variances as an assessment of the analytical model. Since the reference radiance is assumed constant, the measurement error variance is then assumed identical to the measurement variance.

Tabulated in Table 4.1a and Table 4.1b is the percentage error of the calculated local differential average with respect to Δ_V on the 4.67μm and 2.33μm channels respectively. For a quantization length of 16 bits, these results show that error is less than 0.0068% for the 4.67μm channel and less than 0.25% for the 2.33μm channel. The percentage error gets worse at the shorter quantization lengths. This is more noticeable on the 2.33μm channel where Δ_V is comparatively small. For the 4.67μm channel, the greatest percent error is 0.87 percent at 8 bits and on the 2.33μm channel is 44.0151 percent, also at 8 bits.

At a 16 bit quantization length for the 4.67μm channel, the effect of increasing the filter cutoff frequency appears to reduce the error. This result is not as distinct for any other particular cases and the error is increased for the 4.67μm channel at 10 bits. The effect of increasing the sampling frequency does not significantly improve the error for either channel.

Also shown in these tables are the percentage error of the calculated local differential average with respect to Δ_V with ten times the standard deviation of the noise sampled at the zero autocorrelation sampling frequency. On the 4.67μm channel at 16 bits, the error is noticeably smaller at all filter cutoff frequencies. On the 2.33μm channel, the errors are not smaller than the other cases, but the error is reduced with increasing filter cutoff frequency. This improvement in error is believed to be due to the larger number of samples taken at the higher cutoff frequencies.

Tabulated in Table 4.2a and Table 4.2b are the values of the theoretical differential variance of 64 pulse pairs and the sample variance of the local differential averages on the 4.67μm and 2.33μm channels respectively. For the 4.67μm channel at a quantization length of 16 bits, and for all 2.33μm channel cases, these variances closely agree. The sample variance reduces to zero at shorter quantization lengths for most 4.67μm cases, due to the coarser sampling resolution, which makes them difficult to compare to the theoretical values. The close correlation between the sample variances and the theoretical variances suggest that the analytical model is a good representation of the process.

Tabulated in Table 4.3a and Table 4.3b is the percentage error of the calculated collective differential average with respect to Δ_v. The results are consistent with the local differential errors of the 64 pulse pairs tabulated in Tables 4.1a and 4.1b. Again, these results show that for all sampling frequencies, a quantization length of 16 bits provides the smallest error. Some of the error measurements reduce to zero on the 2.33μm channel.

Tabulated in Table 4.4a and Table 4.4b are the theoretical variances for 50 experiments and sample variances of the collective differential measurements. The variances closely coincide at quantization length of 16 bits. Further correlation is noted for all quantization lengths for the 2.33μm channel.

4.4 Evaluation

The analytical results indicated that a quantization length of 16 bits was desired for optimal measurement precision. The simulation results are consistent with this observation for both channels however, a 12 bit quantization length provided better than 1.2% error on both channels for 64 pulse pairs and better than 1.0% for the 50 experiments.

The conjecture that the optimum sampling frequency was the zero autocorrelation frequency also holds true with the simulation results. The results show that the measurement error at the zero autocorrelation sampling frequency are close, and most often less than, the error measurements at higher sampling frequencies. Although the error does not significantly increase with increasing sampling frequency, there is no need to sample faster than necessary.

There was no specific theoretical justification given on the optimal amplifier cutoff frequency. This parameter effects the sampling window and also plays a part in noise attenuation. On the 4.67μm channel at 16 bits, the simulation results show that the effect of cutoff frequency reduces measurement error at $F_c = 10$kHz. Again, this result is consistent an the 2.33μm channel at 12 bits. These results do not lend a clear conclusion on selection of filter cutoff frequency.

4.5 Design Considerations

This investigation reveals several interesting aspects about the measurement process. First, as shown in Tables 3.9a,b,c, the choice of an optimal sampling window will depend upon the cutoff frequency and quantization length. The sampling window must be chosen so that it contributes minimal bias to the measurement. One physical design considerations would be to alter the cell size to obtain a longer view time. This would allow either more samples to be acquired for each pulse or a longer system settling time resulting in less system response ripple.

It has been shown that, with the noise values used, the quantization length should be at least 16 bits on the 4.67μm channel and 12 bits on the 2.33 μm channel. To achieve a measurement error less than 3% as desired, 12 bits is the minimum allowable quantization length as per the results of the simulation for 64 chopper revolutions. However, 16 bits is desired to obtain the most precise measurement.

Fs=Fz

Fc	b=16	b=12	b=10	b=8
2k	0.0052	0.0447	0.1359	0.8662
4k	0.0056	0.0447	0.3185	0.0994
10k	0.0020	0.0293	0.7694	0.1968

Fs=2*Fz

Fc	b=16	b=12	b=10	b=8
2k	0.0068	0.0447	0.2189	0.3915
4k	0.0051	0.0447	0.3185	0.1620
10k	0.0011	0.0338	0.6936	0.2163

Fs=Fb

Fc	b=16	b=12	b=10	b=8
2k	0.0067	0.0426	0.7698	0.0041
4k	0.0052	0.0579	0.7355	0.1825
10k	0.0016	0.0677	0.6328	0.0530

Fs=Fz, 10*stdev of noise

Fc	b=16	b=12	b=10	b=8
2k	0.0018	0.0412	0.1245	0.8662
4k	0.0016	0.0297	0.2843	0.1040
10k	0.0017	0.0078	0.6378	0.1968

Table 4.1a. 4.67μm channel, Absolute Percentage Error of Local Average (volts).

Fs=Fz

Fc	b=16	b=12	b=10	b=8
2k	0.2365	0.6945	10.1243	2.3139
4k	0.2471	1.0464	9.9523	44.0151
10k	0.1860	0.3568	8.8404	15.6436

Fs=2*Fz

Fc	b=16	b=12	b=10	b=8
2k	0.0416	0.7622	10.1243	8.9208
4k	0.0923	0.8322	7.2231	26.6743
10k	0.1170	0.3793	7.0903	22.5305

Fs=Fb

Fc	b=16	b=12	b=10	b=8
2k	0.0562	0.9722	9.3819	17.5571
4k	0.0589	1.1348	9.4721	31.3972
10k	0.0307	0.0502	7.9886	19.9761

Fs=Fz, 10*stdev of noise

Fc	b=16	b=12	b=10	b=8
2k	0.8042	1.0565	1.2439	15.3403
4k	0.2576	0.6954	0.5943	14.2705
10k	0.2783	0.4268	0.6094	1.2885

Table 4.1b. 2.33μm channel, Absolute Percentage Error of Local Average (volts).

Fs=Fz

Fc	b=16	b=12	b=10	b=8
2k	$9.51\cdot10^{-10}$	$1.99\cdot10^{-7}$	$2.65\cdot10^{-6}$	$3.18\cdot10^{-5}$
	$9.45\cdot10^{-10}$	0.0	0.0	0.0
4k	$4.69\cdot10^{-10}$	$8.29\cdot10^{-8}$	$1.14\cdot10^{-6}$	$1.70\cdot10^{-5}$
	$4.34\cdot10^{-10}$	0.0	0.0	0.0
10k	$2.59\cdot10^{-10}$	$3.12\cdot10^{-8}$	$4.54\cdot10^{-7}$	$7.06\cdot10^{-6}$
	$2.56\cdot10^{-10}$	$9.57\cdot10^{-10}$	$1.91\cdot10^{-8}$	0.0

Fs=2*Fz

Fc	b=16	b=12	b=10	b=8
2k	$5.28\cdot10^{-10}$	$1.10\cdot10^{-7}$	$1.45\cdot10^{-6}$	$1.70\cdot10^{-5}$
	$5.41\cdot10^{-10}$	0.0	0.0	0.0
4k	$2.56\cdot10^{-10}$	$4.52\cdot10^{-8}$	$6.11\cdot10^{-7}$	$9.08\cdot10^{-6}$
	$2.07\cdot10^{-10}$	0.0	0.0	0.0
10k	$1.26\cdot10^{-10}$	$1.51\cdot10^{-8}$	$2.18\cdot10^{-7}$	$3.39\cdot10^{-6}$
	$2.12\cdot10^{-10}$	$3.74\cdot10^{-10}$	0.0	0.0

Fs=Fb

Fc	b=16	b=12	b=10	b=8
2k	$1.19\cdot10^{-11}$	$2.48\cdot10^{-9}$	$2.83\cdot10^{-8}$	$4.53\cdot10^{-7}$
	$2.67\cdot10^{-10}$	0.0	$6.61\cdot10^{-11}$	0.0
4k	$1.25\cdot10^{-11}$	$1.86\cdot10^{-9}$	$2.76\cdot10^{-8}$	$4.42\cdot10^{-7}$
	$2.19\cdot10^{-10}$	$5.72\cdot10^{-11}$	$4.32\cdot10^{-11}$	0.0
10k	$1.62\cdot10^{-11}$	$1.83\cdot10^{-9}$	$2.75\cdot10^{-8}$	$4.27\cdot10^{-7}$
	$1.46\cdot10^{-10}$	$3.30\cdot10^{-11}$	$3.39\cdot10^{-10}$	$4.25\cdot10^{-10}$

Fs=Fz, 10*stdev of noise

Fc	b=16	b=12	b=10	b=8
2k	$1.83\cdot10^{-8}$	$2.16\cdot10^{-7}$	$2.66\cdot10^{-6}$	$3.18\cdot10^{-5}$
	$2.17\cdot10^{-8}$	$2.18\cdot10^{-8}$	$1.58\cdot10^{-7}$	0.0
4k	$1.49\cdot10^{-8}$	$9.74\cdot10^{-8}$	$1.15\cdot10^{-6}$	$1.70\cdot10^{-5}$
	$1.91\cdot10^{-8}$	$3.18\cdot10^{-8}$	$5.54\cdot10^{-7}$	$1.06\cdot10^{-7}$
10k	$1.39\cdot10^{-8}$	$4.48\cdot10^{-8}$	$4.67\cdot10^{-7}$	$7.08\cdot10^{-6}$
	$1.38\cdot10^{-8}$	$2.82\cdot10^{-8}$	$4.28\cdot10^{-7}$	0.0

Table 4.2a. 4.67μm channel, Theoretical Variance and Sample Variance over 64 Pulse Pairs.

Fs=Fz

Fc	b=16	b=12	b=10	b=8
2k	$5.26 \cdot 10^{-8}$ $4.46 \cdot 10^{-8}$	$2.51 \cdot 10^{-7}$ $3.11 \cdot 10^{-7}$	$2.69 \cdot 10^{-6}$ $3.36 \cdot 10^{-6}$	$3.18 \cdot 10^{-5}$ $1.93 \cdot 10^{-5}$
4k	$4.36 \cdot 10^{-8}$ $5.54 \cdot 10^{-8}$	$1.26 \cdot 10^{-7}$ $1.77 \cdot 10^{-7}$	$1.17 \cdot 10^{-6}$ $2.05 \cdot 10^{-6}$	$1.70 \cdot 10^{-5}$ $1.87 \cdot 10^{-5}$
10k	$4.10 \cdot 10^{-8}$ $3.20 \cdot 10^{-8}$	$7.19 \cdot 10^{-8}$ $7.45 \cdot 10^{-8}$	$4.92 \cdot 10^{-7}$ $1.23 \cdot 10^{-6}$	$7.10 \cdot 10^{-6}$ $1.07 \cdot 10^{-5}$

Fs=2*Fz

Fc	b=16	b=12	b=10	b=8
2k	$2.92 \cdot 10^{-8}$ $3.38 \cdot 10^{-8}$	$1.39 \cdot 10^{-7}$ $1.40 \cdot 10^{-7}$	$1.47 \cdot 10^{-6}$ $2.00 \cdot 10^{-6}$	$1.70 \cdot 10^{-5}$ $1.24 \cdot 10^{-5}$
4k	$2.37 \cdot 10^{-8}$ $3.97 \cdot 10^{-8}$	$6.87 \cdot 10^{-8}$ $1.34 \cdot 10^{-7}$	$6.31 \cdot 10^{-7}$ $1.20 \cdot 10^{-6}$	$9.10 \cdot 10^{-6}$ $1.22 \cdot 10^{-5}$
10k	$1.99 \cdot 10^{-8}$ $3.25 \cdot 10^{-8}$	$3.49 \cdot 10^{-8}$ $4.39 \cdot 10^{-8}$	$2.36 \cdot 10^{-7}$ $8.10 \cdot 10^{-7}$	$3.41 \cdot 10^{-6}$ $5.44 \cdot 10^{-6}$

Fs=Fb

Fc	b=16	b=12	b=10	b=8
2k	$8.19 \cdot 10^{-10}$ $7.84 \cdot 10^{-8}$	$3.90 \cdot 10^{-9}$ $3.17 \cdot 10^{-7}$	$4.03 \cdot 10^{-8}$ $2.00 \cdot 10^{-6}$	$4.54 \cdot 10^{-7}$ $1.09 \cdot 10^{-5}$
4k	$1.16 \cdot 10^{-9}$ $3.92 \cdot 10^{-8}$	$3.35 \cdot 10^{-9}$ $7.79 \cdot 10^{-8}$	$3.07 \cdot 10^{-8}$ $8.89 \cdot 10^{-7}$	$4.43 \cdot 10^{-7}$ $1.10 \cdot 10^{-5}$
10k	$2.48 \cdot 10^{-9}$ $3.70 \cdot 10^{-8}$	$4.36 \cdot 10^{-9}$ $4.09 \cdot 10^{-8}$	$2.97 \cdot 10^{-8}$ $3.64 \cdot 10^{-7}$	$4.29 \cdot 10^{-7}$ $5.31 \cdot 10^{-6}$

Fs=Fz, 10*stdev of noise

Fc	b=16	b=12	b=10	b=8
2k	$5.18 \cdot 10^{-6}$ $4.55 \cdot 10^{-6}$	$5.38 \cdot 10^{-6}$ $6.38 \cdot 10^{-6}$	$6.97 \cdot 10^{-6}$ $6.35 \cdot 10^{-6}$	$3.50 \cdot 10^{-5}$ $4.37 \cdot 10^{-5}$
4k	$4.32 \cdot 10^{-6}$ $4.72 \cdot 10^{-6}$	$4.41 \cdot 10^{-6}$ $5.43 \cdot 10^{-6}$	$4.84 \cdot 10^{-6}$ $4.80 \cdot 10^{-6}$	$2.04 \cdot 10^{-5}$ $2.37 \cdot 10^{-5}$
10k	$4.09 \cdot 10^{-6}$ $4.18 \cdot 10^{-6}$	$4.12 \cdot 10^{-6}$ $4.59 \cdot 10^{-6}$	$4.19 \cdot 10^{-6}$ $4.48 \cdot 10^{-6}$	$1.07 \cdot 10^{-5}$ $9.31 \cdot 10^{-6}$

Table 4.2b. 2.33µm channel, Theoretical Variance and Sample Variance over 64 Pulse Pairs.

Fs=Fz

Fc	b=16	b=12	b=10	b=8
2k	0.0058	0.0447	0.1359	0.8662
4k	0.0054	0.0447	0.3185	0.0994
10k	0.0020	0.0300	0.7696	0.1968

Fs=2*Fz

Fc	b=16	b=12	b=10	b=8
2k	0.0066	0.0447	0.2189	0.3915
4k	0.0050	0.0447	0.3185	0.1620
10k	0.0009	0.0336	0.6937	0.2163

Fs=Fb

Fc	b=16	b=12	b=10	b=8
2k	0.0065	0.0426	0.7698	0.0041
4k	0.0049	0.0581	0.7355	0.1825
10k	0.0015	0.0677	0.6328	0.0531

Fs=Fz, 10*stdev of noise

Fc	b=16	b=12	b=10	b=8
2k	0.0019	0.0419	0.1249	0.8662
4k	0.0009	0.0311	0.2909	0.1003
10k	0.0009	0.0065	0.6438	0.1968

Table 4.3a. 4.67μm channel, Absolute Percentage Error for the Collective Average.

Fs=Fz

Fc	b=16	b=12	b=10	b=8
2k	0.0038	0.9177	9.5519	2.3941
4k	0.0112	0.8508	9.4892	41.4729
10k	0.0247	0.1746	7.5264	18.4826

Fs=2*Fz

Fc	b=16	b=12	b=10	b=8
2k	0.0003	0.8617	9.0242	7.2988
4k	0.0018	0.8922	9.3607	30.0699
10k	0.0030	0.2176	7.4386	22.9157

Fs=Fb

Fc	b=16	b=12	b=10	b=8
2k	0.0084	0.7862	9.5520	17.2600
4k	0.0011	0.7705	9.9250	31.5889
10k	0.0081	0.1855	7.5188	20.8221

Fs=Fz, 10*stdev of noise

Fc	b=16	b=12	b=10	b=8
2k	0.0274	0.2467	0.1445	9.0811
4k	0.1636	0.1460	0.0280	15.4475
10k	0.3211	0.2222	0.6259	3.2126

Table 4.3b. 2.33μm channel, Absolute Percentage Error for the Collective Average.

Fs=Fz

Fc	b=16	b=12	b=10	b=8
2k	$1.486 \cdot 10^{-11}$	$3.107 \cdot 10^{-9}$	$4.139 \cdot 10^{-8}$	$4.967 \cdot 10^{-7}$
	$1.144 \cdot 10^{-11}$	0.0	$1.12 \cdot 10^{-15}$	0.0
4k	$7.331 \cdot 10^{-12}$	$1.296 \cdot 10^{-9}$	$1.774 \cdot 10^{-8}$	$2.649 \cdot 10^{-7}$
	$6.592 \cdot 10^{-12}$	0.0	0.0	0.0
10k	$4.050 \cdot 10^{-12}$	$4.872 \cdot 10^{-10}$	$7.098 \cdot 10^{-9}$	$1.104 \cdot 10^{-7}$
	$4.222 \cdot 10^{-12}$	$2.019 \cdot 10^{-11}$	$1.82 \cdot 10^{-5}$	0.0

Fs=2*Fz

Fc	b=16	b=12	b=10	b=8
2k	$8.255 \cdot 10^{-12}$	$1.726 \cdot 10^{-9}$	$2.258 \cdot 10^{-8}$	$2.650 \cdot 10^{-7}$
	$9.310 \cdot 10^{-12}$	0.0	0.0	0.0
4k	$3.999 \cdot 10^{-12}$	$7.068 \cdot 10^{-10}$	$9.553 \cdot 10^{-9}$	$1.419 \cdot 10^{-7}$
	$5.682 \cdot 10^{-12}$	0.0	0.0	0.0
10k	$1.964 \cdot 10^{-12}$	$2.362 \cdot 10^{-10}$	$3.403 \cdot 10^{-9}$	$5.298 \cdot 10^{-8}$
	$3.260 \cdot 10^{-12}$	$9.681 \cdot 10^{-12}$	$1.115 \cdot 10^{-12}$	0.0

Fs=Fb

Fc	b=16	b=12	b=10	b=8
2k	$1.853 \cdot 10^{-13}$	$3.874 \cdot 10^{-11}$	$4.427 \cdot 10^{-10}$	$7.083 \cdot 10^{-9}$
	$4.589 \cdot 10^{-12}$	$2.290 \cdot 10^{-14}$	$7.123 \cdot 10^{-13}$	0.0
4k	$1.946 \cdot 10^{-13}$	$2.912 \cdot 10^{-11}$	$4.320 \cdot 10^{-10}$	$6.911 \cdot 10^{-9}$
	$6.396 \cdot 10^{-12}$	$1.010 \cdot 10^{-12}$	$8.570 \cdot 10^{-13}$	$1.384 \cdot 10^{-13}$
10k	$2.536 \cdot 10^{-13}$	$2.861 \cdot 10^{-11}$	$4.291 \cdot 10^{-10}$	$6.667 \cdot 10^{-9}$
	$3.051 \cdot 10^{-12}$	$4.109 \cdot 10^{-13}$	$4.900 \cdot 10^{-12}$	$5.817 \cdot 10^{-12}$

Fs=Fz, 10*stdev of noise

Fc	b=16	b=12	b=10	b=8
2k	$2.853 \cdot 10^{-10}$	$3.378 \cdot 10^{-9}$	$4.162 \cdot 10^{-8}$	$4.969 \cdot 10^{-7}$
	$1.698 \cdot 10^{-10}$	$2.400 \cdot 10^{-10}$	$2.851 \cdot 10^{-9}$	0.0
4k	$2.330 \cdot 10^{-10}$	$1.521 \cdot 10^{-9}$	$1.793 \cdot 10^{-8}$	$2.651 \cdot 10^{-7}$
	$2.513 \cdot 10^{-10}$	$3.760 \cdot 10^{-10}$	$4.912 \cdot 10^{-9}$	$2.703 \cdot 10^{-10}$
10k	$2.174 \cdot 10^{-10}$	$7.006 \cdot 10^{-10}$	$7.293 \cdot 10^{-9}$	$1.106 \cdot 10^{-7}$
	$2.638 \cdot 10^{-10}$	$5.366 \cdot 10^{-10}$	$5.888 \cdot 10^{-9}$	0.0

Table 4.4a. 4.67μm channel, Theoritical Variance and Sample Variance over 50 Experiments.

Fs=Fz

Fc	b=16	b=12	b=10	b=8
2k	$8.220\cdot10^{-10}$	$3.914\cdot10^{-9}$	$4.207\cdot10^{-8}$	$4.972\cdot10^{-7}$
	$7.586\cdot10^{-10}$	$4.092\cdot10^{-9}$	$4.968\cdot10^{-8}$	$2.668\cdot10^{-7}$
4k	$6.805\cdot10^{-10}$	$1.969\cdot10^{-9}$	$1.832\cdot10^{-8}$	$2.654\cdot10^{-7}$
	$5.778\cdot10^{-10}$	$2.756\cdot10^{-9}$	$2.697\cdot10^{-8}$	$2.612\cdot10^{-7}$
10k	$6.408\cdot10^{-10}$	$1.124\cdot10^{-9}$	$7.680\cdot10^{-9}$	$1.109\cdot10^{-7}$
	$6.641\cdot10^{-10}$	$1.347\cdot10^{-9}$	$1.199\cdot10^{-8}$	$1.217\cdot10^{-7}$

Fs=2*Fz

Fc	b=16	b=12	b=10	b=8
2k	$4.567\cdot10^{-10}$	$2.175\cdot10^{-9}$	$2.295\cdot10^{-8}$	$2.652\cdot10^{-7}$
	$9.927\cdot10^{-10}$	$2.581\cdot10^{-9}$	$3.747\cdot10^{-8}$	$1.932\cdot10^{-7}$
4k	$3.712\cdot10^{-10}$	$1.074\cdot10^{-9}$	$9.864\cdot10^{-9}$	$1.422\cdot10^{-7}$
	$6.787\cdot10^{-10}$	$2.144\cdot10^{-9}$	$2.280\cdot10^{-8}$	$2.406\cdot10^{-7}$
10k	$3.107\cdot10^{-10}$	$5.450\cdot10^{-10}$	$3.682\cdot10^{-9}$	$5.325\cdot10^{-8}$
	$4.062\cdot10^{-10}$	$9.896\cdot10^{-10}$	$6.494\cdot10^{-9}$	$8.224\cdot10^{-8}$

Fs=Fb

Fc	b=16	b=12	b=10	b=8
2k	$1.280\cdot10^{-11}$	$6.097\cdot10^{-11}$	$6.294\cdot10^{-10}$	$7.090\cdot10^{-9}$
	$9.747\cdot10^{-10}$	$1.809\cdot10^{-9}$	$4.147\cdot10^{-8}$	$2.529\cdot10^{-7}$
4k	$1.807\cdot10^{-11}$	$5.227\cdot10^{-11}$	$4.803\cdot10^{-10}$	$6.925\cdot10^{-9}$
	$4.626\cdot10^{-10}$	$1.706\cdot10^{-9}$	$1.760\cdot10^{-8}$	$2.039\cdot10^{-7}$
10k	$3.884\cdot10^{-11}$	$6.812\cdot10^{-11}$	$4.640\cdot10^{-10}$	$6.701\cdot10^{-9}$
	$4.195\cdot10^{-10}$	$8.370\cdot10^{-10}$	$8.852\cdot10^{-9}$	$8.937\cdot10^{-8}$

Fs=Fz, 10*stdev of noise

Fc	b=16	b=12	b=10	b=8
2k	$8.100\cdot10^{-8}$	$8.409\cdot10^{-8}$	$1.088\cdot10^{-7}$	$5.473\cdot10^{-7}$
	$7.449\cdot10^{-8}$	$7.716\cdot10^{-8}$	$1.307\cdot10^{-7}$	$7.577\cdot10^{-7}$
4k	$6.755\cdot10^{-8}$	$6.884\cdot10^{-8}$	$7.564\cdot10^{-8}$	$3.189\cdot10^{-7}$
	$6.873\cdot10^{-8}$	$6.374\cdot10^{-8}$	$6.220\cdot10^{-8}$	$3.990\cdot10^{-7}$
10k	$6.389\cdot10^{-8}$	$6.438\cdot10^{-8}$	$6.551\cdot10^{-8}$	$1.672\cdot10^{-7}$
	$5.432\cdot10^{-8}$	$6.397\cdot10^{-8}$	$5.248\cdot10^{-8}$	$1.429\cdot10^{-7}$

Table 4.4b. 2.33μm channel, Theoritical Variance and Sample Variance over 50 Experiments.

CHAPTER FIVE

CONCLUSIONS

5.1 Assessment

The goal of this thesis is to develop a simulation model for the TRACER gas correlation radiometer. Based on the empirical results presented in Chapter Four, we believe this goal has been achieved within the limits of actual information about the system. There are no established results with which to compare this model. It stands on its own merits as a step in developing a digital signal processing technique to measure the mean of input radiance.

The fact that the theoretical and empirical sample variances were in close agreement gives confidence that the model is accurate. It is unfortunate that the detector and preamplifier models could not be supported by authentic data from an actual detector and amplifier. These models are considered to be the weakest elements of this study, yet they constitute a large part of the signal conditioning. This limits the analysis to the point of estimating the response of selected parameters with a given input signal and noise value. However, the results of

Chapter Four show agreement with the theoretical model providing validity to the digital processing portion of the model.

The analytical model addressed the issues of selecting optimal quantization length, sampling frequency, and amplifier cutoff frequency. While implementing the simulation model, it became apparent that the choice of a suitable quantization length was dependent upon the expected signal noise variance at the A/D input. In turn, the noise variance depends to some degree on the amplifier cutoff frequency, the system gain, and certain other system parameters. For the signal values under consideration, the theoretical quantization length was determined to be 16 bits for the 4.67μm channel and (greater than) 12 bits for the 2.33μm channel. The simulation results are consistent with this conclusion. The analytical model also showed that the optimal sampling frequency was the 'zero autocorrelation' frequency for each filter cutoff selection. The simulation results show that sampling faster than the 'zero autocorrelation' frequency does not improve the measurement estimate. Thus, it is not desirable to sample faster than this frequency. Definite conclusions as to selection of amplifier cutoff frequency cannot be clearly drawn from the simulation results.

5.2 Future Research

If future research like that reported in this thesis is to continue it will be necessary to better define the detector and preamplifier models, or to utilize actual data as input to the signal processing module. Since there are so many possible parameters in a good detector model, this should be a study all in itself. Existing detector models are theoretical in nature and are based on specific characteristics of the detector material. There have been intensive detector models developed, yet they generally only account for a very specific type of detector.

Another future research consideration is to examine the selection of a sampling window based on system response and quantization length. This was done in Chapter Three, however a detailed investigation may provide other valuable insights.

Future research needs to consider that the input radiance, unfortunately, may not remain constant during the instrument viewing time. For areas where this radiance may not be constant, a means of discerning and interpreting the radiance fluctuation must be established.

REFERENCES

[1] "Tropospheric Radiometer For Atmospheric Chemistry and Environmental Research (TRACER) A Multi-level Carbon Monoxide Correlation Radiometer," Instrument Investigation Proposal, NASA, Vol. 1, July 1988.

[2] "Carbon Monoxide in the Atmosphere," W. Seiler and L. E. Junge, J. Geophys. Res., vol 75, 1970, p.2217-2226.

[3] "Measurement of Air Pollutants from Satellites. 1: Feasibility Considerations," C. B. Ludwig et al., Applied Optics, June 1974, p.1494-1509.

[4] Global Tropospheric Chemistry: A Plan for Action, National Academy Press, Washington D.C., 1984, p.123-124.

[5] "Feasibility of Determining the vertical profile of carbon monoxide from a space platform," H. Reichle Jr., et. al., Applied Optics, June 1989, p.2104-2110.

[6] E. Dereniak and D. Crowe, Optical Radiation Detectors, Wiley & Sons, New York, 1984.

[7] A. V. Oppenheim and R. W. Schafer, Digital Signal Processing, Prentice-Hall, New Jersey, 1975.

[8] S. Park, Lecture Notes on Probability, College of William and Mary, CS 426/526, Version 1, July 1988.

[9] I. Guttman, Introductory Engineering Statistics, John Wiley & Sons, Inc., New York, 1971.

[10] P. Z. Peebles, Probability, Random Variables, and Random Signal Principles, McGraw-Hill Book Co., New York, 1980.

[11] G. R. Cooper and C. D. McGillem, Probabilistic Methods of Signal and System Analysis, Holt, Rinehart and Wilson, Inc., New York, 1971.

[12] F. G. Stremler, Introduction to Communication Systems, Addison-Welsley Publishing Co., Reading, Mass., 1982.

[13] A. Papoulis, Probability, Random Variables, and Stochastic Processes, McGraw-Hill Book Co., New York, 1984.